Supplementary Information

Anti-electrowetting carbon film electrode with self-sustained aeration for industrial H_2O_2 electrosynthesis

Lele Cui[1,2†], Bin Chen[3,4†], Longshun Zhang[3†], Chen He[3], Chen Shu[3], Hongyu Kang[1,2], Jian Qiu[3,4], Wenheng Jing[3]*, Kostya (Ken) Ostrikov[5], and Zhenghua Zhang[1,2,5]*

[1]Membrane & Nanotechnology-Enabled Water Treatment Center, Institute of Environment and Ecology, Guangdong Provincial Engineering Research Centre for Urban Water Recycling and Environmental Safety, Tsinghua Shenzhen International Graduate School, Tsinghua University, Shenzhen 518055, China

[2]School of Environment, Tsinghua University, Beijing 100084, China

[3]State Key Laboratory of Materials-Oriented Chemical Engineering, Nanjing Tech University, 5 Xinmofan Road, Nanjing 210009, China

[4]Jiangsu Shuangliang Environmental Technology Co., Ltd, Jiangyin 214400, China

[5]Australian Research Council (ARC) Centre of Excellence for Carbon Science and Innovation (ARC-CoE), Queensland Node, School of Chemistry and Physics and QUT Centre for Materials Science, Queensland University of Technology (QUT), Brisbane, Queensland 4000, Australia.

[†]These authors contributed equally to this work.

*Corresponding author: jingwh@njtech.edu.cn; zhenghua.zhang@sz.tsinghua.edu.cn

Materials and Methods

Chemicals and materials

Carbon black (CB) (Vulcan XC-72) and polytetrafluoroethylene (PTFE) (60%) were supplied by Shanghai Aladdin Biological Technology Co., Ltd. Stainless steel mesh (SSM) and nickel foam (NF) were provided by Kunshan TengErHui Electronic Technology Co., Ltd. Graphite felt (GF) was purchased from Shanghai Hongjun Industry Co., Ltd. 39BB and W1S1011 gas diffusion layers (GDLs) were purchased from Sigracet and CeTech, respectively. Ti/RuO_2-IrO_2 plate, Ti/RuO_2-IrO_2 mesh, and Ti/Pt mesh were purchased from Suzhou Shuertai Industrial Technology Co., Ltd. Anhydrous sodium sulfate (Na_2SO_4, 99%) and potassium titanium (IV) oxalate ($K_2TiO(C_2O_4)_2$, ≥98%) were purchased from Shanghai Macklin Biochemical Co., Ltd. All the chemicals were of analytical grade unless otherwise specified.

Fabrication of structurally continuous and discontinuous electrodes

Simplified from the traditional sandwich-like gas diffusion electrode (GDE), the electrodes used in this work were all double-layer structures including a CB-PTFE functional layer and a SSM (or NF, GF) substrate. Specifically, the cleaned SSM was soaked in the PTFE suspension (5 wt%) for 30 min and then taken out and dried at room temperature before use. For CB-PTFE layer with different spatial structures, CB particles were ultrasonically dispersed in anhydrous ethanol for 10 min, followed by the dropwise addition of PTFE (at a CB-to-PTFE mass ratio of 5:3) and vigorous stirring at 70 °C until a wet paste was formed. The resulting paste was uniformly coated on one side of SSM with CB loading of 12.44, 24.88, and 37.32 mg/cm^2, and

calcined at 350 °C for 60 min. During this process, many cracks formed in the plate structure due to the volume shrinkage caused by the rapid volatilization of ethanol, which was named as a discontinuous CB-PTFE film (DCP). As a control group, the CB-PTFE paste and SSM were placed in a mold, cold-pressed at 18 MPa for 10 min, and annealed at 350 °C for 60 min to obtain a traditional flat surface electrode with the same CB loading as DCP, which was named as a continuous CB-PTFE film (CCP).

Characterization

Scanning electron microscopy (SEM) was performed on a Hitachi S4800 field emission scanning electron microscope. X-ray diffraction (XRD) spectra were collected on an X-ray diffractometer (Rigaku MiniFlex 600) with a Cu Kα radiation ($\lambda = 0.154$ nm). The contact angles of different electrodes were recorded using a contact angle instrument (DropMeterA-100P). The surface roughness was measured using a laser microscope (VK-X3000, Keyence). The electrical conductivity of CCP and DCP electrodes was measured by using a standard four-point probe method (4 Probes Tech, RTS-9). The chemical state of carbon on the electrode surface was studied by X-ray photoelectron spectroscopy (XPS) (Thermo Scientific K-Alpha Nexsa).

Electrochemical H_2O_2 Production

Electrochemical O_2-to-H_2O_2 tests were performed in a custom-made undivided electrolyzer containing 100 mL of 0.05 M Na_2SO_4 as a supporting electrolyte, with its initial pH adjusted using 1 M H_2SO_4 or NaOH. Galvanostatic measurements were

performed using a Reference 3000 electrochemical workstation (Gamry Instruments, USA). The DCP/CCP (30 mm in diameter) and a Pt foil (10 mm × 10 mm × 0.1 mm), placed at a mutual distance of 20 mm, were used as cathode and anode, respectively. During the entire electrolysis process, the exposed SSM side of the cathode faced the air, without the assistance of any external aeration equipment. Aliquots of the solution (1 mL) were collected from the reactor at pre-established time points and analyzed to determine the H_2O_2 concentration. All error bars represent the standard deviation of three independent measurements.

Determination of H_2O_2 concentration

The concentration of the produced H_2O_2 was determined by a UV-vis spectrophotometer (UV759, Shanghai Instrument Analysis Instrument Co., Ltd) using the potassium titanium (IV) oxalate method at λ = 400 nm. The standard curve for H_2O_2 determination was plotted with the H_2O_2 concentration as *x*-axis and the absorbance value at 400 nm as *y*-axis, as shown in Fig. S4. Potassium titanium (IV) oxalate can react with H_2O_2 to form a stable yellow-orange titanium (IV)-peroxide complex, with its color depth being proportional to the H_2O_2 concentration.[1] In detail, 1 mL of sample and 1 mL of chromogenic agent were mixed evenly and then diluted to 10 mL for testing. The current efficiency (CE) for H_2O_2 electrosynthesis was calculated through the following equation:

$$CE(\%) = \frac{nFCV}{It} \times 100\% \quad \text{(S1)}$$

where n is the number of electrons transferred for O_2 reduction to H_2O_2 (n = 2), F is the Faraday constant (96486 C/mol), C is the concentration of H_2O_2 (mol/L), V is the

volume of electrolyte (L), I is the current (A), and t is the electrolysis time (s).

Electrocatalytic performance analysis

All electrochemical performance analysis experiments were carried out in the electrosynthesis H_2O_2 electrolyzer using the same electrochemical workstation. A three-electrode system was established using the prepared DCP or CCP as the working electrode, a Pt sheet as the counter electrode and an Ag/AgCl (or Hg/HgO) electrode as the reference electrode. Linear sweep voltammetry (LSV) curves were collected at a scan rate of 20 mV/s over a potential window of 0 to −1.6 V in Na_2SO_4 (0.05 M) solution. Electrochemical impedance spectroscopy (EIS) was conducted under an open circuit potential in Na_2SO_4 (0.05 M) electrolyte solution, with a frequency range from 10^5 to 10^{-2} Hz and an amplitude of 5 mV. EIS data were fitted using ZView software with an appropriate equivalent circuit. Electrochemically active surface area (ECSA) of different electrodes was determined by conducting cyclic voltammetry (CV) measurements at 20, 40, 60, 80, and 100 mV/s in a potential window where only double-layer charging and discharging occur, specifically between −0.1 V vs. Hg/HgO and 0.1 V vs. Hg/HgO. 0.1 M deoxygenated KOH was used as the supporting electrolyte. The double-layer capacitance (C_{dl}) was estimated by plotting the $\Delta j = (j_a - j_c)/2$ at 0 V vs. Hg/HgO against the scan rate. The ECSA value was calculated from the equation: ECSA = $C_{dl} \div C_s \times S$, where C_s is the specific capacitance of a flat standard electrode with 1 cm^2 of real surface area (determined to be 40 μF/cm^2 according to several previous studies[2,3]), S is the actual geometric area of the electrode. The ORR selectivity and activity of CB in the DCP electrode

structure were evaluated using rotating ring-disk electrode (RRDE) (Pine Instruments, USA) technique. Specifically, LSV was performed in an O_2-saturated KOH (0.1 M) solution between −1.0 and 0.2 V, at a scan rate of 10 mV/s and a rotation speed of 1600 rpm with a ring potential of 0.6 V.

Finite element method (FEM) modeling

FEM-based theoretical calculations were performed on COMSOL Multiphysics with the same procedure as in the previous work.[4] To simplify the theoretical model, we constructed four characteristic 2D models including DCP electrodes with different crack widths and a plane DCP electrode without any cracks. The detailed geometric dimensions of these models were shown in Fig. S21. The electric field (E) distribution was described by the following equation:

$$E = -\nabla V \quad \text{(S2)}$$

$$\rho = \varepsilon_r \varepsilon_0 \nabla \cdot E \quad \text{(S3)}$$

where V, ρ, ε_0, and ε_r represent the applied potential bias, charge density, dielectric constant of vacuum and materials, respectively.

The mentioned equations were solved in a steady state according to the previous work.[4] In this study, to ensure the high accuracy of the simulation results, the densest conventional triangular meshes were used for all simulations on the electrode surface and the MUMPS solver was used.

Molecular dynamics (MD) simulations

A periodic eight-layer graphite (001) was used to represent the CCP hydrophobic surface, and the same model was cut to form a 2.6 nm width slit-like pore without a

closed end to represent the DCP electrode. The radius of the initial water droplet was set to 2.5 nm with a total number of water molecules of 2208, corresponding to the pure water density of 1 g/cm^3. Both models were 93.7 × 91.0 × 320.0 Å^3 (X × Y × Z), accompanied by a parallel graphite wall 279.1 Å away from the upper surface of the models in the Z axis. Periodic boundary conditions were applied to these simulation boxes, ensuring that graphite surfaces were infinitely large in the X and Y directions. A constant charge method was employed to simulate the electric field exerting to the system along the Z axis, where a charge of 0.001 e was assigned to each of the total 3256 C atoms in the graphite wall. Meanwhile, the same amount of negative charges was allocated evenly to the first layer of C atoms within the two models to neutralize the system and form an electric field (Fig. S22). A 500 ps NVT ensemble MD simulation was performed at 298.15 K to obtain information on the wettability evolution of water droplets in each system.

In this work, PACKMOL was used to construct the model systems.[5] LAMMPS was used to perform all the molecular simulations.[6] The PCFF force field was used to simulate the interaction of different constituents.[7] To capture electrostatic and van der Waals interactions in the system, PPPM summation and atom-based summation with a cutoff of 12 Å were employed. During the simulations, the integration time step was fixed at 1.0 fs using the Verlet velocity algorithm. The temperature was controlled by the Nosé-Hoover thermostat.[8] Equations of motions were integrated using the Verlet velocity method and the atomic coordinates were saved every 1.0 ps for post-analysis.

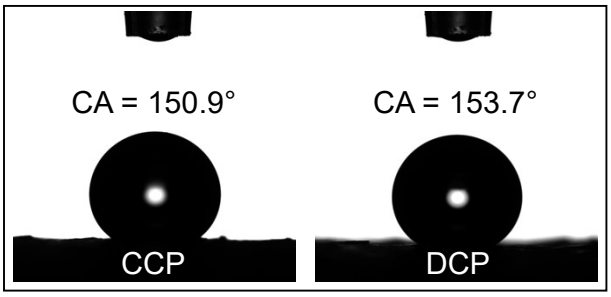

Fig. S1 Water contact angle measurement of CCP and DCP film electrodes.

The water contact angles (θ) of the CCP and DCP electrodes were identified to be 150.9° and 153.7°, respectively, both within the category of superhydrophobicity (θ >150°).[9]

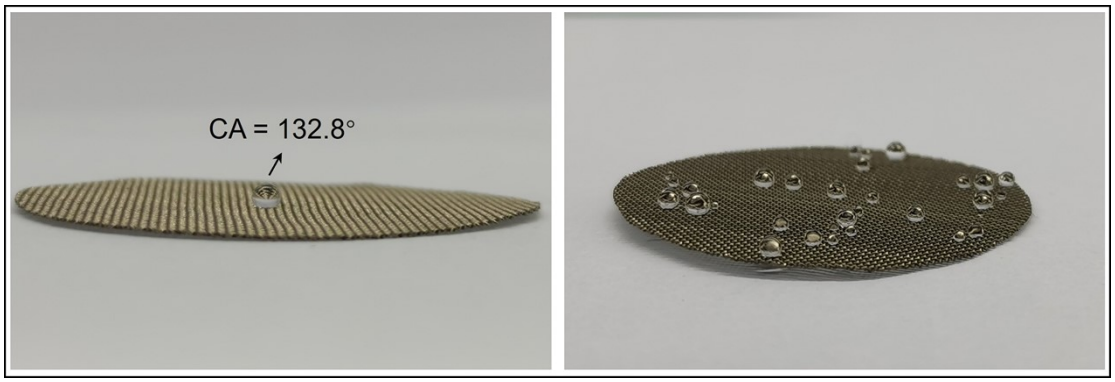

Fig. S2 Hydrophobicity of PTFE-treated SSM.

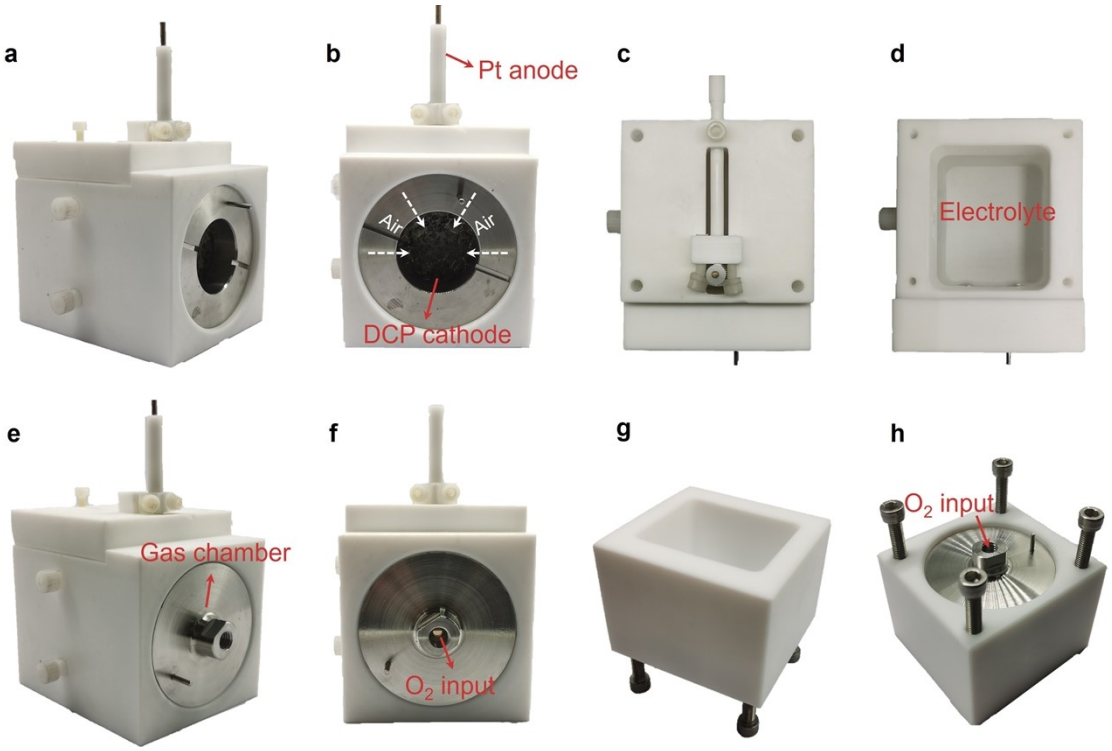

Fig. S3 Experimental setup for *in-situ* electrochemical production of H_2O_2. (a−d) Photos of an electrolyzer with the working electrode exposed to the atmosphere. (e) and (f) Photos of an electrolyzer with a gas chamber for the pure O_2 aeration experimental system. (g) and (h) Photos of an electrolyzer used to monitor bubble evolution behavior on the electrolyte-facing side of CCP or DCP electrode operated under pure O_2 aeration.

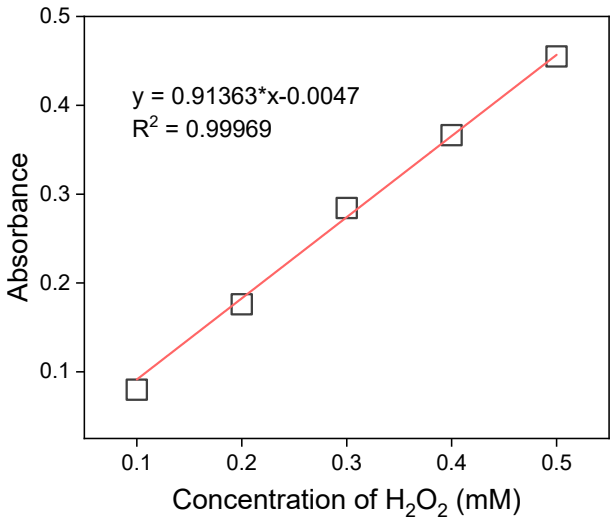

Fig. S4 Standard curve of absorbance values versus H_2O_2 concentration.

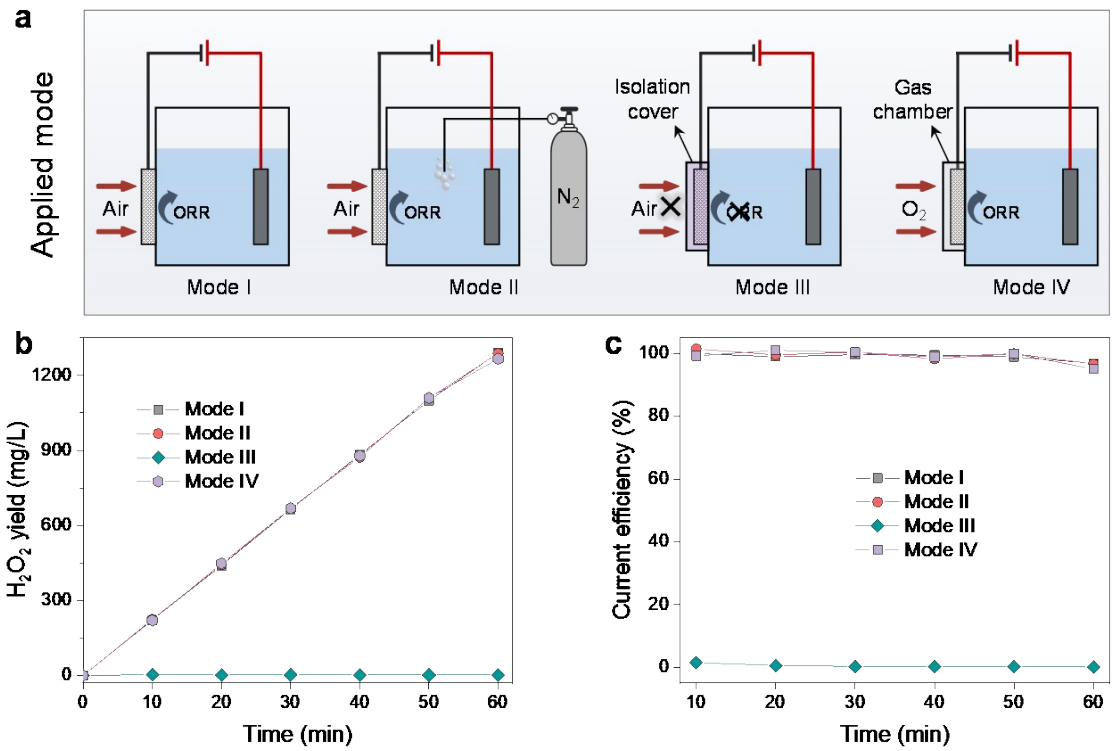

Fig. S5 O_2 source control experiments in the H_2O_2 production process using DCP electrode. (a) Schematic illustration of different H_2O_2 production modes applied (Mode I: with the DCP facing air; Mode II: with the DCP facing the air and the electrolyte bubbling N_2; Mode III: with the DCP not exposed to air; Mode IV: with the DCP exposed to high-pressure pure O_2 flow). (b) H_2O_2 yield and (c) the corresponding CE.

When the air-facing side of the DCP was shielded with an isolation cover (Mode III), almost no H_2O_2 was detected with a CE of only 0.15%. This result is puzzling because the transfer of anode-evolved O_2 to the cathode is possible in our undivided cell (unlike flow cells equipped with proton exchange membranes), which would contribute to the potential H_2O_2 production. To further strengthen the reliability of the experimental results of Mode III, the DCP was exposed to air while N_2 was bubbled into the electrolyte (Mode II) to eliminate any interference caused by non-air O_2

(dissolved O_2 or anode-evolved O_2). Interestingly, the H_2O_2 production in Mode II (96.7%) did not decrease and was almost equivalent to that in Mode I (96.9%). In addition, when pure O_2 supply was implemented (Mode IV), it can be found that the accumulation of H_2O_2 (1266.6 mg/L) and the corresponding CE (95.1%) were also similar to those of Model I (1291.1 mg/L, 96.9%). Therefore, we can safely conclude that the O_2 consumed by the DCP electrode during the production of H_2O_2 is almost entirely from the air.

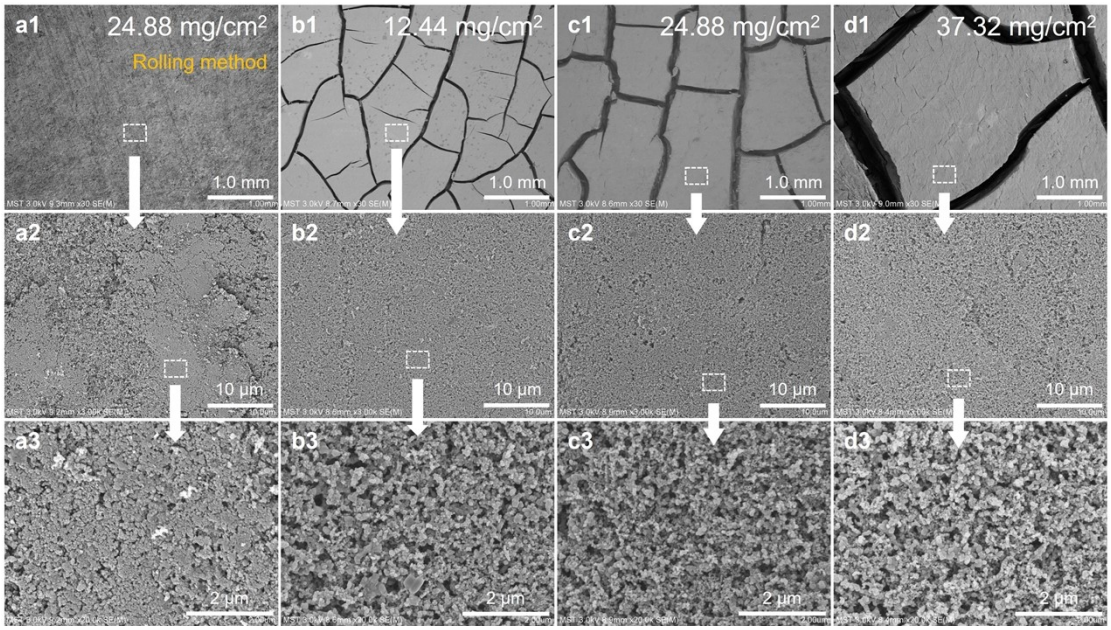

Fig. S6 Morphology of CCP and DCP electrodes with different CB loadings. (a) CCP electrode and (b−d) DCP electrode.

It can be observed that the dense regions of all DCP electrodes exhibit a rougher and larger pore structure than that of CCP at the micron scale (2 μm).

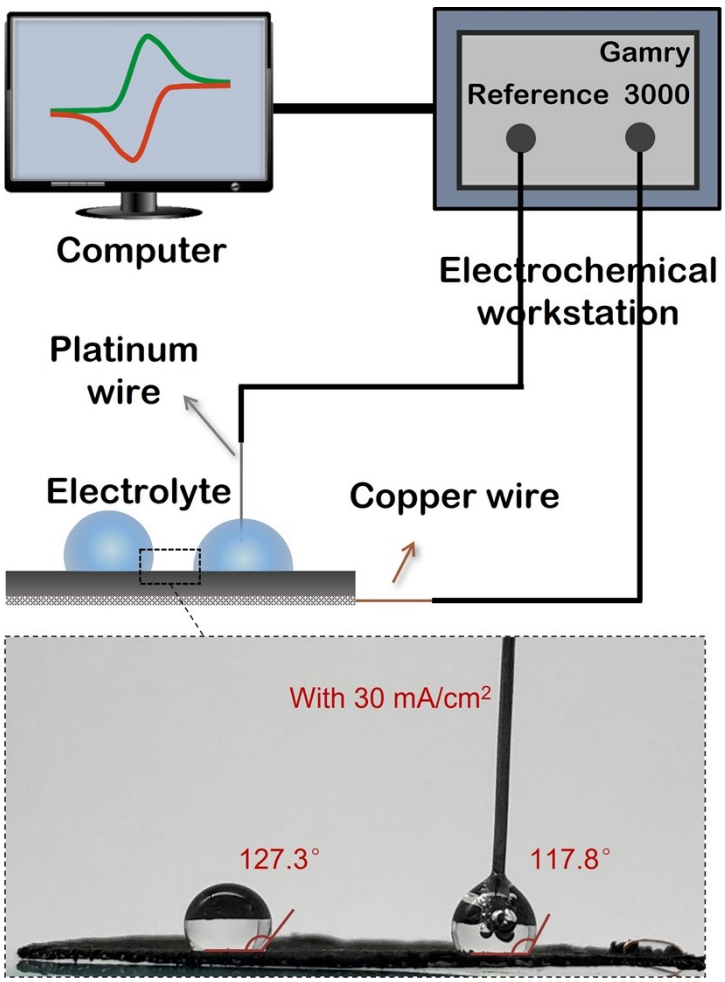

Fig. S7 Visualization of the electrowetting effect. The contact angle change of the electrolyte droplet on the CCP electrode was monitored in real time at a current density of 30 mA/cm^2 on a custom-made device.

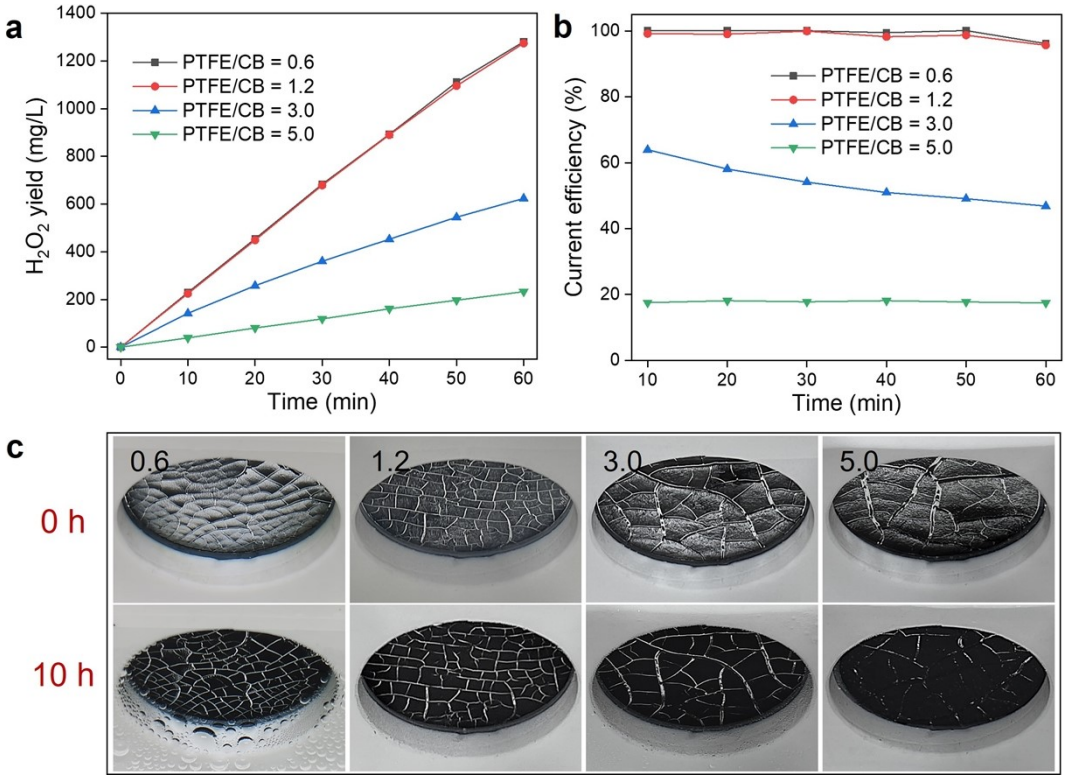

Fig. S8 Effect of PTFE binder content in electrode on interface wettability and H_2O_2 generation performance. (a) H_2O_2 yield and (b) CE of the electrodes at different PTFE/CB ratios. (c) Interfacial wettability evolution of different electrodes after 10 h of reaction.

The yield of H_2O_2 began to decrease as the PTFE/CB ratio was higher than 3, probably because the excess PTFE not only shielded the carbon active sites but also slowed down the electron transport due to its insulating properties.[10]

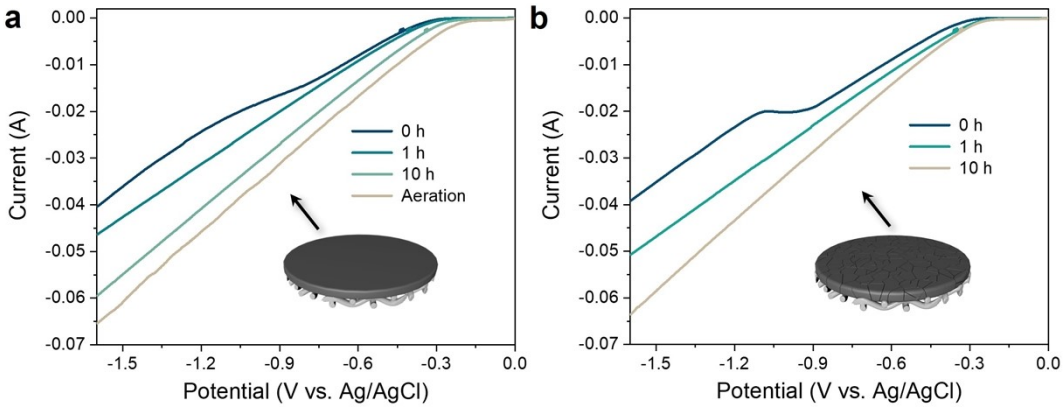

Fig. S9 Electrochemical characterization of different electrodes. LSV curves of (a) CCP and (b) DCP electrodes at different cycle numbers under real reaction conditions.

Note that all LSV tests in this work were performed in the H_2O_2-producing electrolyzer without any aeration process (N_2 or O_2) for the electrolyte, which is believed to reflect the ORR electrocatalytic behavior of the electrode under real electrolysis conditions. In addition, we consider that for such gas-involving electrodes, the response current of LSV may be the result of multiple factors rather than just the ORR performance. For example, in the case of DCP and CCP electrodes, the response currents increased with the increase of the number of cycles. However, the $2e^-$ ORR performance of the CCP electrode was instead deteriorated (decreased H_2O_2 yield as revealed in Fig. 2(a) of the main text), suggesting that the significantly enhanced LSV response current was attributed to the increased electroactive surface area caused by the continuous electrolyte penetration into the cathode. According to the experimental results in the main text, the hydrophilic transition of the CCP electrode is more serious after 10 h of reaction, so it is expected that the response current of CCP should be higher than that of DCP at the same potential. However, the results showed that the

corresponding value of DCP (24 mA) was higher than that of CCP (20 mA) at −0.75 V, indicating that the rapid diffusion of O_2 in the crack also leads to the enhanced response current. This is further confirmed by the slightly enhanced response current after applying pure O_2 aeration to the hydrophilic CCP electrode after 10 h of reaction, due to the enhanced forced convection of O_2 in the CCP pores.

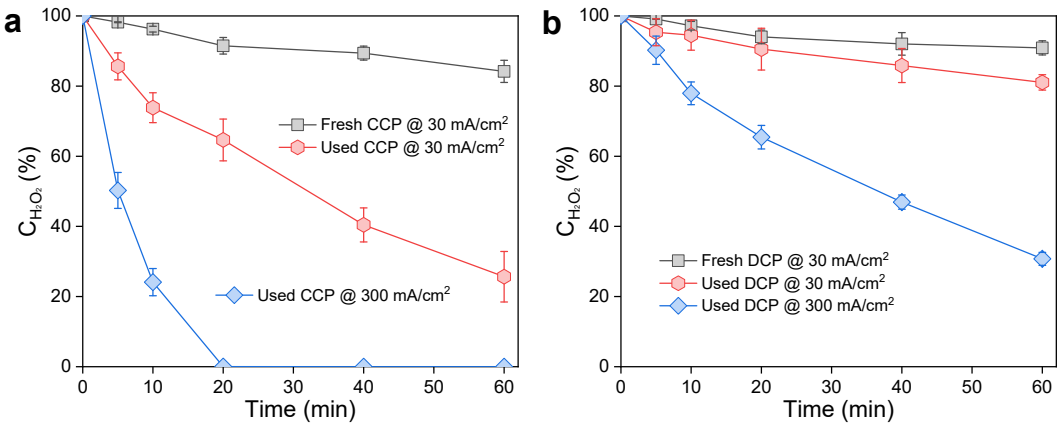

Fig. S10 Reductive decomposition of H_2O_2 by (a) CCP and (b) DCP electrodes with different wettability at different operating current densities (conditions: [H_2O_2] = 1000 mg/L, H-type cell, 0.05 M N_2-saturated Na_2SO_4).

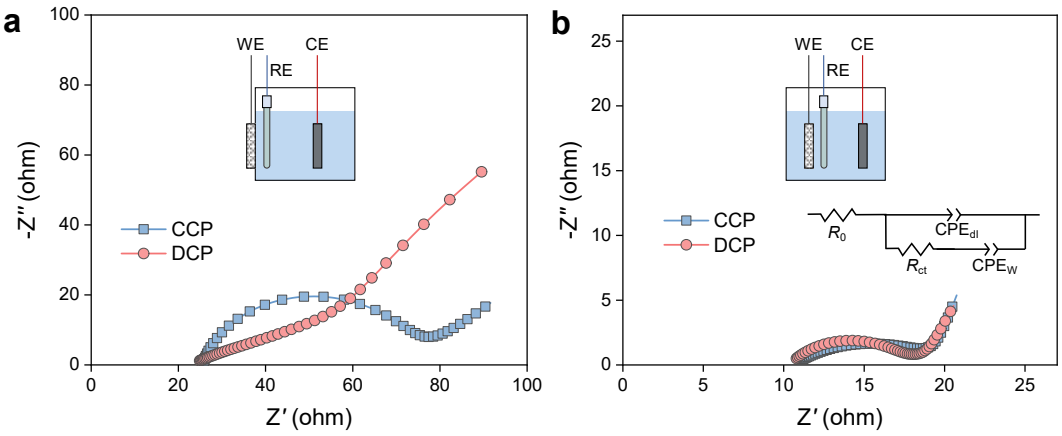

Fig. S11 Nyquist plots of CCP and DCP electrodes (a) exposed to open air or (b) immersed in N_2-saturated electrolyte (inset: a simplified equivalent circuit model, R_0: ohmic resistance of electrolyte and electrode; R_{ct}: charge transfer resistance; CPE: constant phase element).

We also examined the interfacial electrochemical reaction impedance of DCP and CCP electrodes after 10 h of reaction at catalytically relevant conditions in the same H_2O_2-producing electrolyzer by means of EIS. The impedance here is therefore likely due to the overlapping responses of charge transport and mass transport impedance during $2e^-$ ORR.[11] It can be observed from Fig. S11a that the charge transfer resistance toward the $2e^-$ ORR of the DCP electrode (26.8 Ω) is much lower than that of the CCP electrode (48.3 Ω), consistent with the LSV results at −0.75 V. However, control EIS measurements performed with DCP and CCP electrodes directly immersed in N_2-saturated electrolytes showed their comparable charge transfer resistances (7.3 Ω for DCP and 9.5 Ω for CCP), probably due to their similar O_2 mass-transfer behavior (both characterized as sluggish) under this condition. The overall smaller impedance values of the working electrode immersed in the electrolyte compared to its exposure to open air may be due to the larger contact area of the

electrode with the electrolyte in the former case. The above facts collectively underscore the crucial role of unblocked O_2 transport channels in accelerating interfacial charge transfer and O_2-to-H_2O_2 conversion performance, similar to previously reported electrochemical gas-consuming reactions that prefer hydrophobic-aerophilic microenvironments.[12,13]

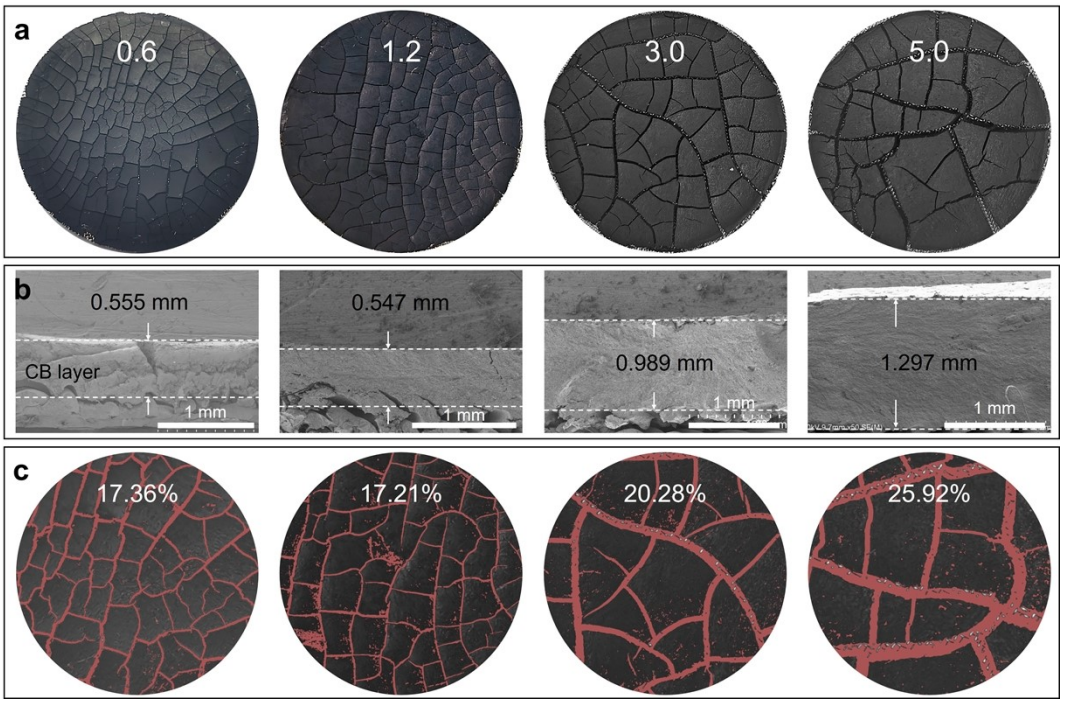

Fig. S12 Tuning of parameters of cracks in DCP electrode structure. (a) Optical images, (b) active layer thickness (i.e., crack depth), and (c) crack density statistics (estimated using ImageJ software) of DCP electrodes fabricated at PTFE/CB ratios of 0.6, 1.2, 3.0, and 5.0.

Both the crack depth and crack density in the DCP structure exhibited a positive correlation with the PTFE/CB ratio. This may be attributed to the fact that the increase in PTFE content will lead to an increase in the volume of CB-PTFE wet paste, which not only complicates the coating process but also aggravates the uneven solvent evaporation rate within the coating.

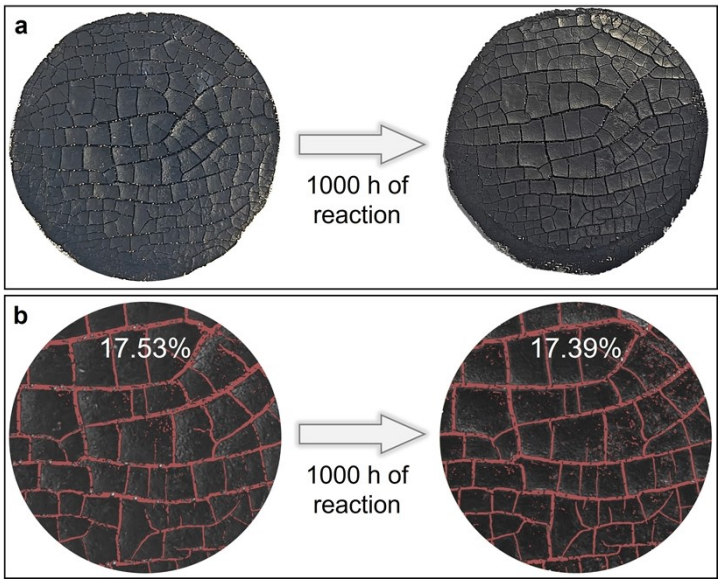

Fig. S13 Structural stability of DCP electrode. (a) Optical images and (b) crack density statistics of DCP electrodes before and after continuous reaction for 1000 h.

The optimized DCP electrode (i.e., CB loading of 24.88 mg/cm^2) did not experience any structural disintegration and catalyst plate shedding after approximately 1000 h of continuous operation, even though it was frequently disassembled and cleaned during the process.

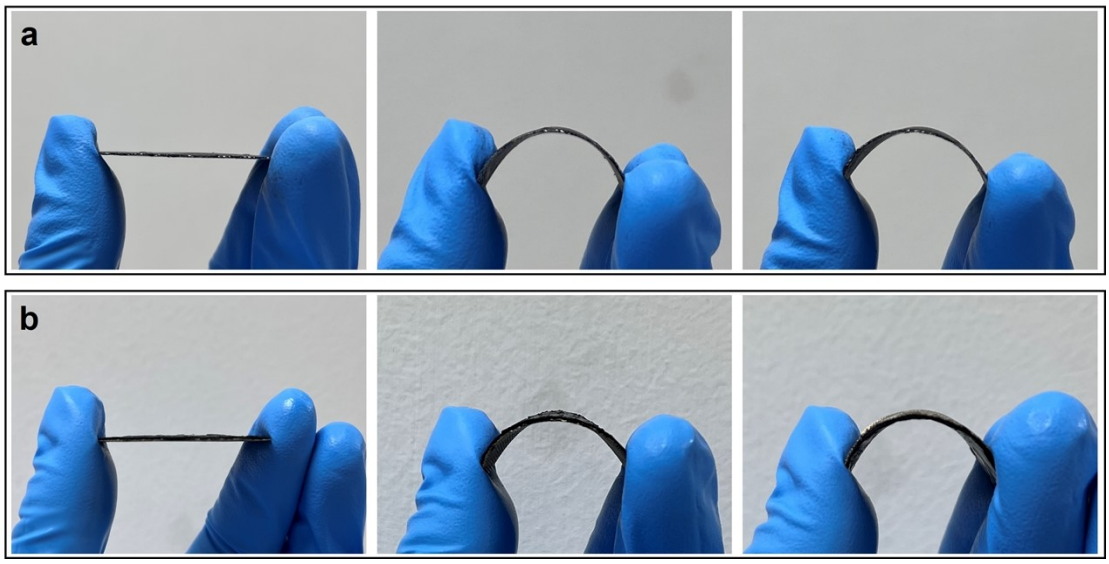

Fig. S14 Comparison of mechanical properties of CCP and DCP electrodes (CB loading of 24.88 mg/cm^2). Optical images of (a) CCP and (b) DCP electrodes bending in different directions.

We artificially bend the DCP electrode to demonstrate its feasible mechanical properties. As shown in Fig. S14, similar to CCP, the CB plate in the active layer of DCP did not show any delamination from the stainless-steel mesh substrate and breakage into small pieces of debris even under severe bending deformation. Therefore, we believe that the DCP electrode can operate stably under real working conditions without damage.

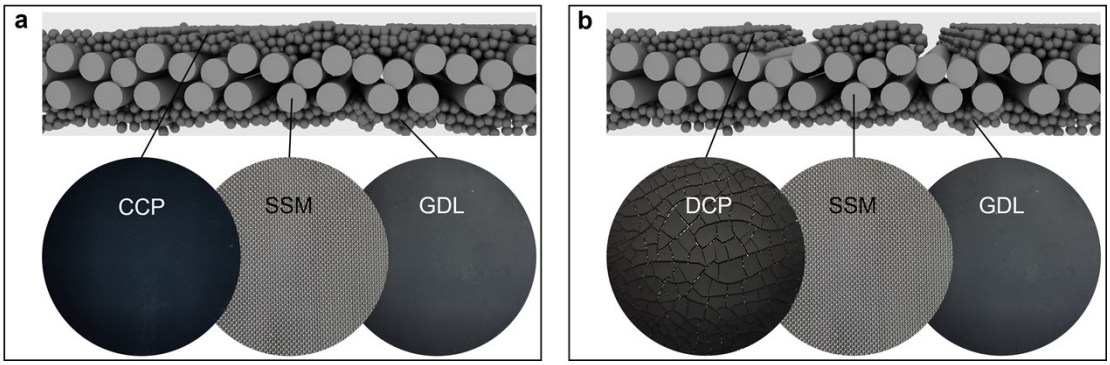

Fig. S15 Schematics and photos of the traditional sandwich-type GDE configurations: (a) “CCP + GDL” and (b) “DCP + GDL”.

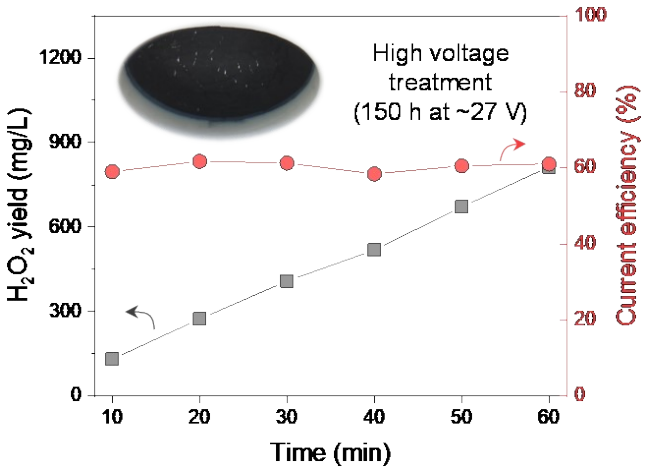

Fig. S16 The key role of cracks on the discontinuous electrode in the O_2-to-H_2O_2 conversion process. H_2O_2 production performance of hydrophilic "DCP + GDL" electrode obtained by long-term high-voltage treatment.

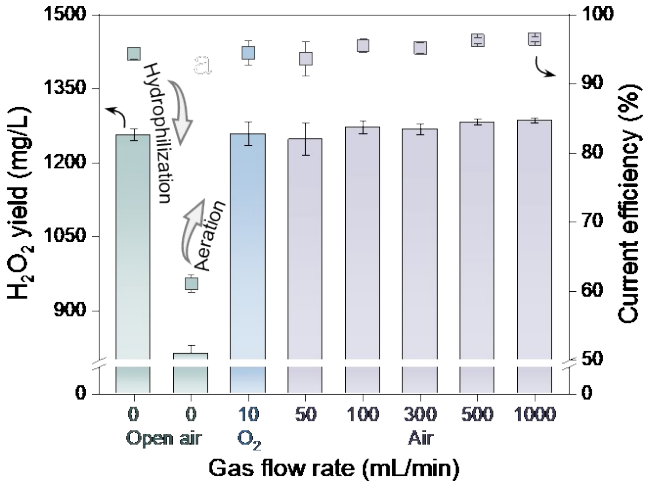

Fig. S17 H_2O_2 production performance of hydrophilic "DCP + GDL" electrode with pure O_2 or air aeration.

We additionally performed a series of H_2O_2 production experiments with hydrophilic "DCP + GDL" electrode under air aeration conditions. When air with a flow rate >50 mL/min was introduced into the additionally deployed gas chamber in the electrolysis system, considerable irregular air bubbles were observed to appear on the surface of the electrolyte-facing side of the "DCP + GDL" electrode. This enhanced gas convection is beneficial to increase the local air/O_2 concentration at the wetting interface of the "DCP + GDL" electrode, thereby enabling the recovery of its H_2O_2 production performance. As shown in Fig. S17, similar to the case of pure O_2 aeration, the hydrophilic "DCP + GDL" electrode operated with air aeration (50–1000 mL/min) also exhibited comparable H_2O_2 yield and CE to the hydrophobic "DCP + GDL" electrode operated in the open air. These results further highlight the critical role of unobstructed gas-accessible channels in $2e^-$ ORR reactions (especially for open air systems), which is largely controlled by the hydrophobicity at the electrode-electrolyte interface.

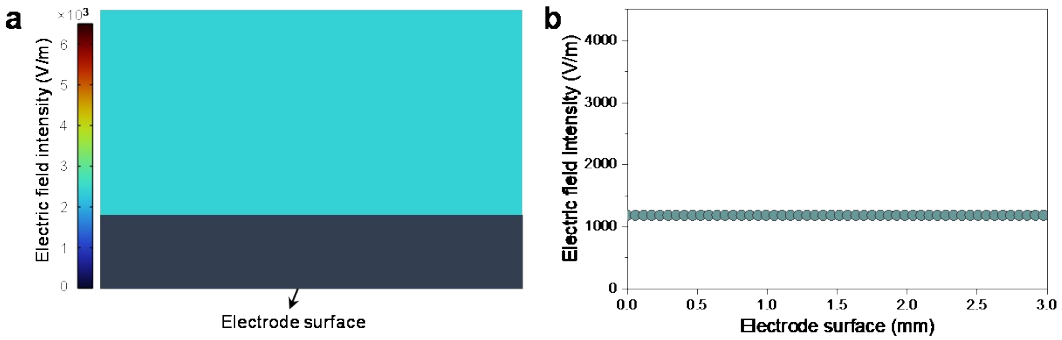

Fig. S18 COMSOL simulation of electric field distribution. (a) Simulation results of electric field distribution on the CCP electrode surface. (b) Quantification of the electric field at the CCP electrode-electrolyte interface.

It can be found that the electric field is uniformly distributed at the interface of the CCP electrode due to its flat and regular catalyst film.

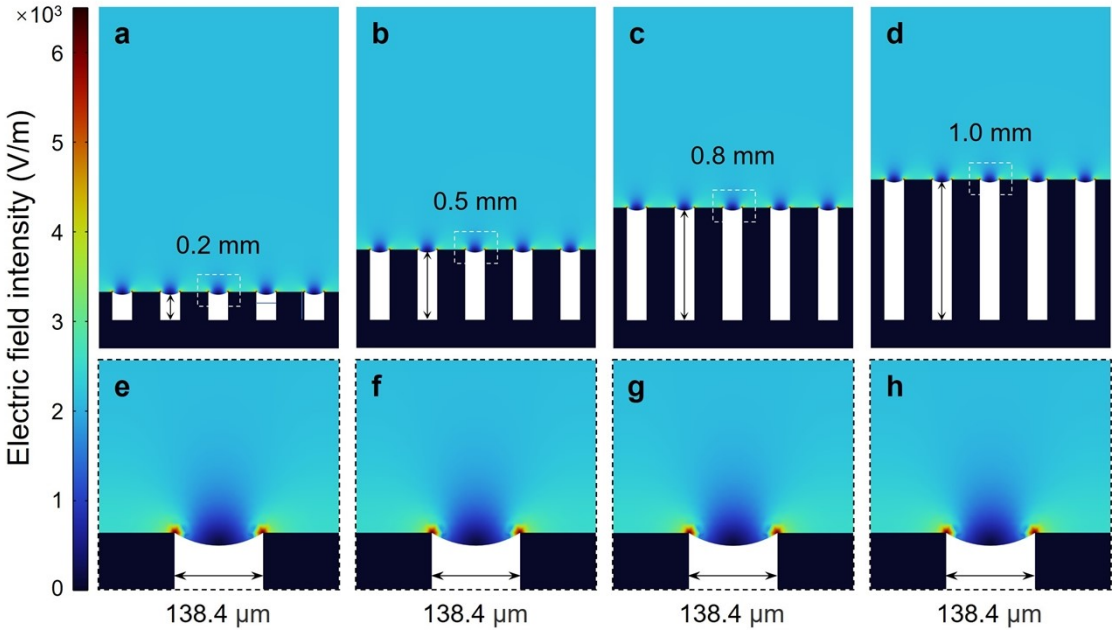

Fig. S19 Effect of crack depth on electric field distribution. COMSOL simulation of the electric field distribution in the electrolyte near the electrode surface with different crack depths: (a) and (e) 0.2 mm; (b) and (f) 0.5 mm; (c) and (g) 0.8 mm; (d) and (h) 1.0 mm.

As long as the crack width is fixed (138.4 μm as an example, i.e., the crack width of a DCP electrode with a CB loading of 24.88 mg/cm^2), varying the crack depth from 0.2 mm to 1.0 mm seems to hardly affect the electric field profile at the DCP electrode interface. We have demonstrated in the main text that the overall robust hydrophobicity and anti-electrowetting effect of the DCP electrode effectively limits the penetration of electrolyte into the cracks. The electric field distribution at the electrode-electrolyte interface is therefore considered to be independent of the depth of the crack since the electric field exists only in the outermost solid region of the DCP electrode accessible to the electrolyte.

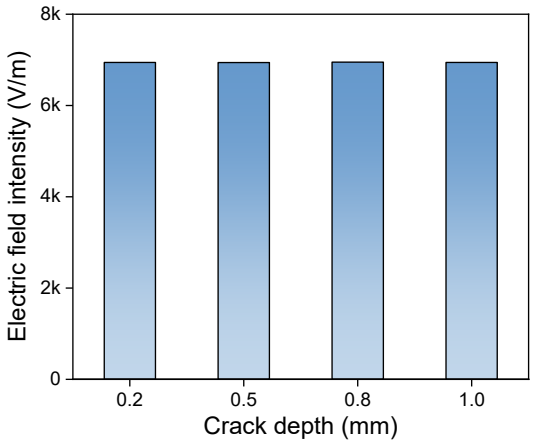

Fig. S20 Quantified electric field intensity near the edge of the crack with different depths.

The similar electric field intensity values at the edges of cracks with different depths further demonstrate that crack depth cannot affect the electrocatalytic behavior at the solid-liquid interface of DCP.

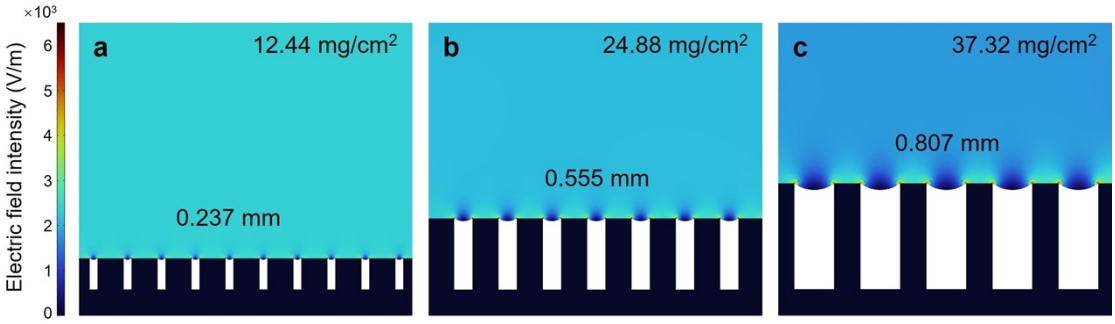

Fig. S21 Electric field distribution at the interface of DCP electrodes with different CB loadings. According to the real DCP electrode model, different crack widths correspond to different crack depths.

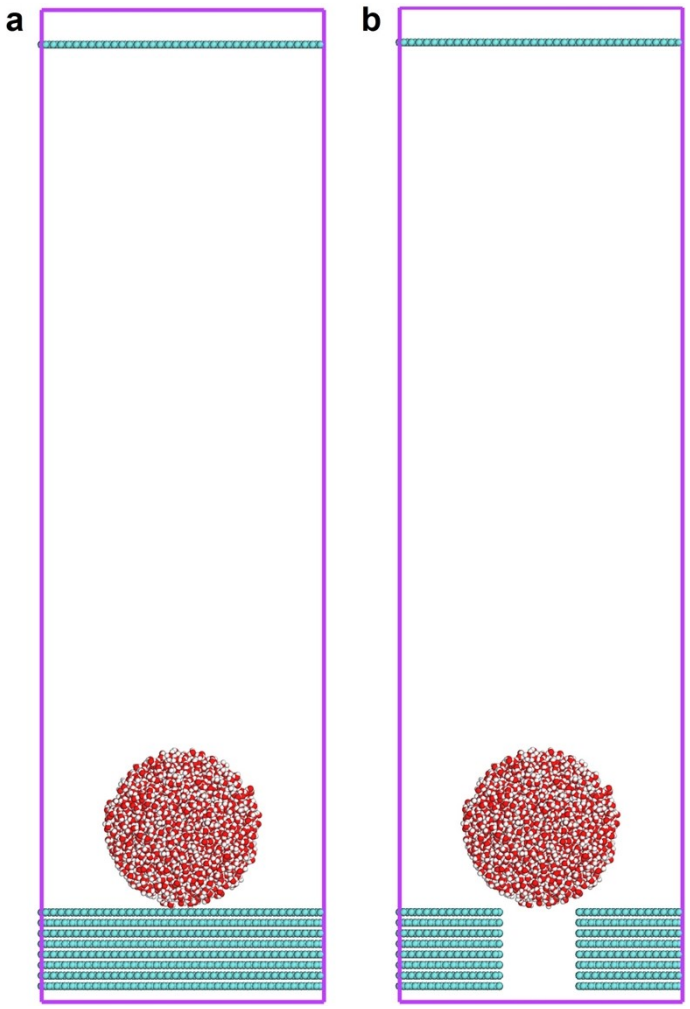

Fig. S22 MD simulations. Schematic illustration of the simulation system for (a) CCP and (b) DCP electrode models (side-view). C, cyan; H, white; O, red.

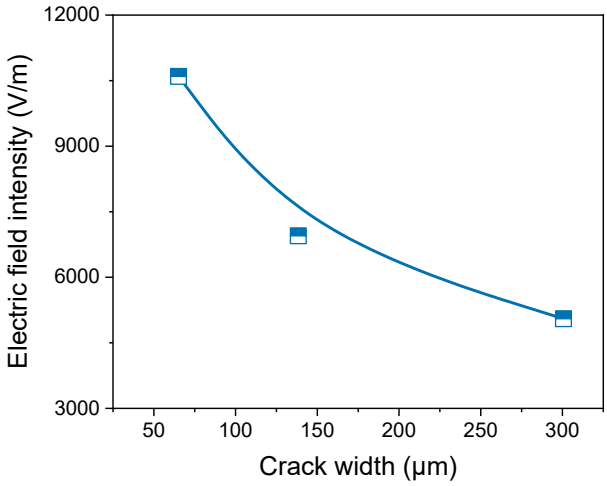

Fig. S23 Electric field "hot spot" phenomenon at the crack edge. Fitting curves of electric field intensity near the edge of the crack with different widths.

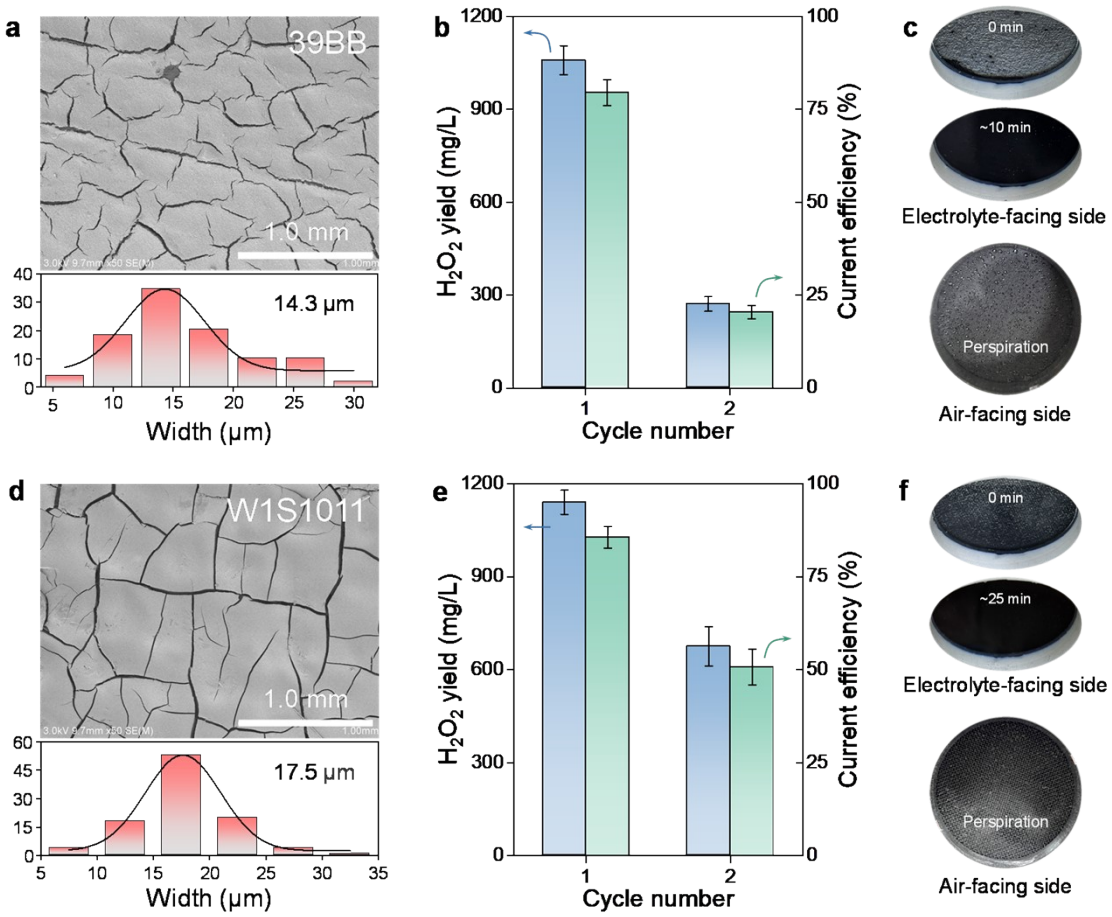

Fig. S24 H_2O_2 production performance of commercial bare GDL at 30 mA/cm^2. (a) SEM image and (b) H_2O_2 yield of 39BB, as well as (c) its wettability evolution during operation. (d) SEM image and (e) H_2O_2 yield of W1S1011, as well as (f) its wettability evolution during operation.

We selected two different commercial GDLs (39BB and W1S1011) for control experiments, both of which are bilayer structures composed of carbon fiber support (carbon paper for 39BB and carbon cloth for W1S1011) and microporous layer (MPL). Abundant cracks with average widths of 14.3 μm and 17.5 μm were observed in the MPL structures of 39BB and W1S1011, respectively (Fig. S24a and d). The H_2O_2 production performance of different GDLs was examined in the same undivided electrolyzer utilized in the main text. Both pristine 39BB and W1S1011 exhibit

underwater hydrophobicity and an obvious air film can be observed at the electrode-electrolyte interface (Fig. S24c and f). Nevertheless, the H_2O_2 accumulation and CE of these two GDLs were unsatisfactory in the first cycle and rapidly decayed to 20.4% (39BB) and 50.7% (W1S1011) in the second cycle (Fig. S24b and e). This phenomenon can be attributed to the fact that the cracks in the two GDL structures cannot effectively overcome electrowetting, as demonstrated in Fig. S24c and f that the interfacial hydrophobicity of 39BB and W1S1011 was completely lost (even electrolyte perspiration occurred) after 10 and 25 min of reaction. The slightly better H_2O_2 production performance of W1S1011 compared to 39BB may be attributed to its enhanced hydrophobicity endowed by the additional PTFE treatment (reflected by insignificant electrolyte perspiration on the air-facing side of the electrode). The crack widths in 39BB (14.3 μm) and W1S1011 (17.5 μm) structures (invisible to the naked eye) are much smaller than 65.1 μm (visible to the naked eye), the lowest crack width value for the DCP electrodes we investigated. Therefore, the edges of these tiny cracks in the 39BB and W1S1011 structures will be distributed with ultra-high local electric field strength, thereby accelerating the electrowetting effect and the evolution of interfacial hydrophilicity. Therefore, controlling the crack size within an appropriate range (~138.4 μm) is critical for the implementation of the concept of anti-electrowetting carbon film electrode with self-sustained aeration.

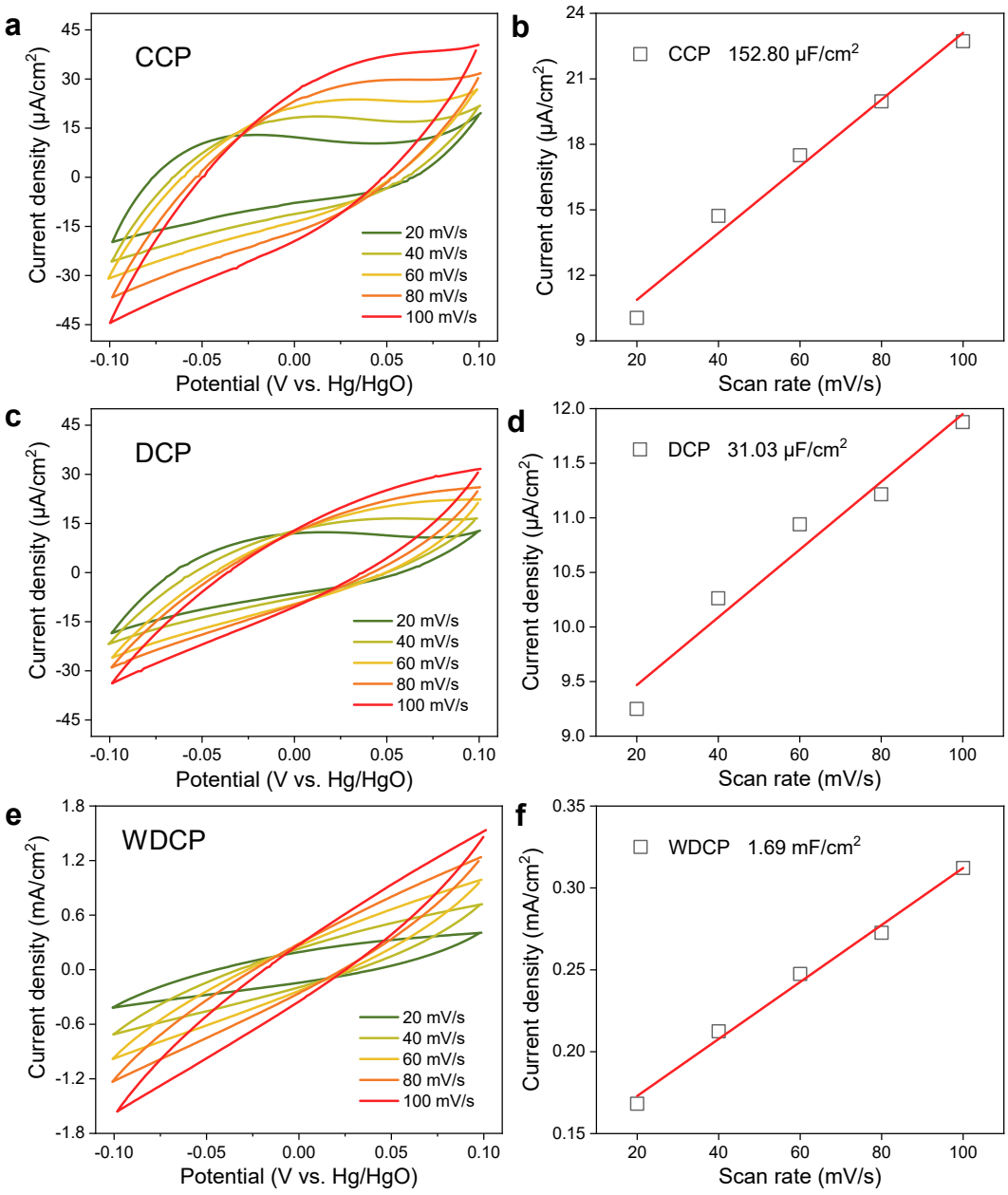

Fig. S25 Determination of C_{dl} for different electrodes. CV curves recorded at 20, 40, 60, 80, and 100 mV/s of (a) CCP, (c) DCP, and (e) wetted DCP (WDCP, i.e., DCP with the hydrophobicity at the cracks destroyed by long-period high-voltage operation, Fig. S16). Current density at 0.00 V for (b) CCP, (d) DCP, and (f) WDCP as a function of CV scan rate and the fitted C_{dl} value for each electrode.

The ECSA of different electrodes is positively related with the C_{dl} value and ranks following the order WDCP > CCP > DCP. This result is reasonable because

ECSA represents the area of an electrode that is wetted and accessible to the electrolyte.[14] In addition, the higher ECSA of the CCP electrode than the DCP electrode can be explained by the electrochemical inertness at the crack region of the DCP electrode.

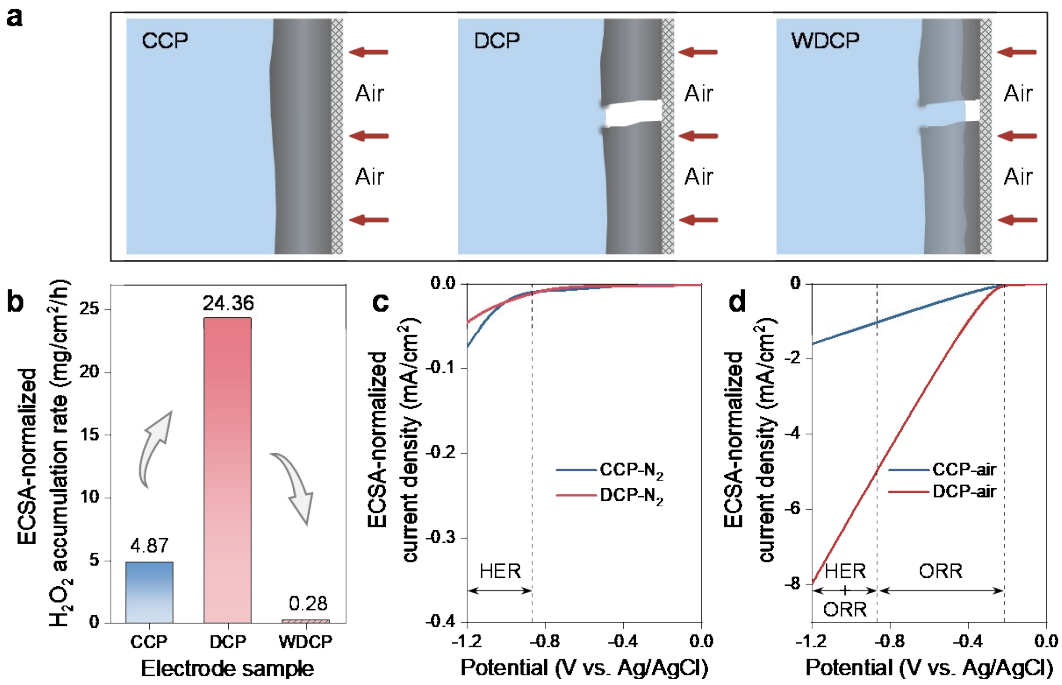

Fig. S26 The critical role of crack edges in accelerating O_2-to-H_2O_2 conversion. (a) Schematic illustration of electrosynthesis of H_2O_2 with CCP, DCP and WDCP electrodes. (b) Comparison of ECSA-normalized H_2O_2 accumulation rates of CCP, DCP, and WDCP electrodes. ECSA-normalized LSV curves of CCP and DCP electrodes under (c) N_2 and (d) air atmospheres.

Notably, the ECSA-normalized H_2O_2 production rate of the DCP electrode (24.36 mg/cm^2/h) largely exceeded that of the CCP electrode (4.87 mg/cm^2/h) at 30 mA/cm^2, despite their comparable CE (97.85% for CCP and 99.30% for DCP) and electrode geometric area-normalized H_2O_2 production rate (18.62 mg/cm^2/h for CCP and 18.89 mg/cm^2/h for DCP), suggesting that cracks play an important role in accelerating O_2-to-H_2O_2 conversion. We further examined the LSV curves of DCP and CCP under N_2 or air atmosphere (Fig. S26c and d). The obtained ECSA-normalized LSV curves indicated that the presence of cracks in the film architecture could not affect the intrinsic activity of the DCP electrode in terms of $2e^-$ ORR, as

evidenced by the nearly identical ORR onset potentials of CCP and DCP.[15] Note that the higher current increase rate of DCP than CCP at more negative potentials was mainly attributed to the crack-induced accelerated O_2 reactant diffusion kinetics.[16] Based on the above analysis, we therefore consider that the ECSA-normalized H_2O_2 productivity enhancement of DCP might be largely attributed to the local high electric field at the crack edge (tip effect). In addition, unblocked and rapid O_2 transport within the crack void was identified as equally important for the realization of this hot spot-induced strengthening effect. For example, once the crack is fully flooded with electrolyte, the ECSA-normalized H_2O_2 production rate of the WDCP electrode (0.28 mg/cm^2/h, Fig. S26b) drops significantly (even lower than that of the CCP), even with the locally high electric field at the crack edge (Fig. S26a). Overall, the local high electric field at the crack edge can increase the utilization efficiency of active sites by rapidly depleting O_2 reactants, while the crack voids allow rapid air transport to replenish O_2 to the crack edge in time. Therefore, this interaction enables the stable and efficient production of H_2O_2 by significantly altering the reaction kinetics at the crack edge rather than the intrinsic activity of the electrode.

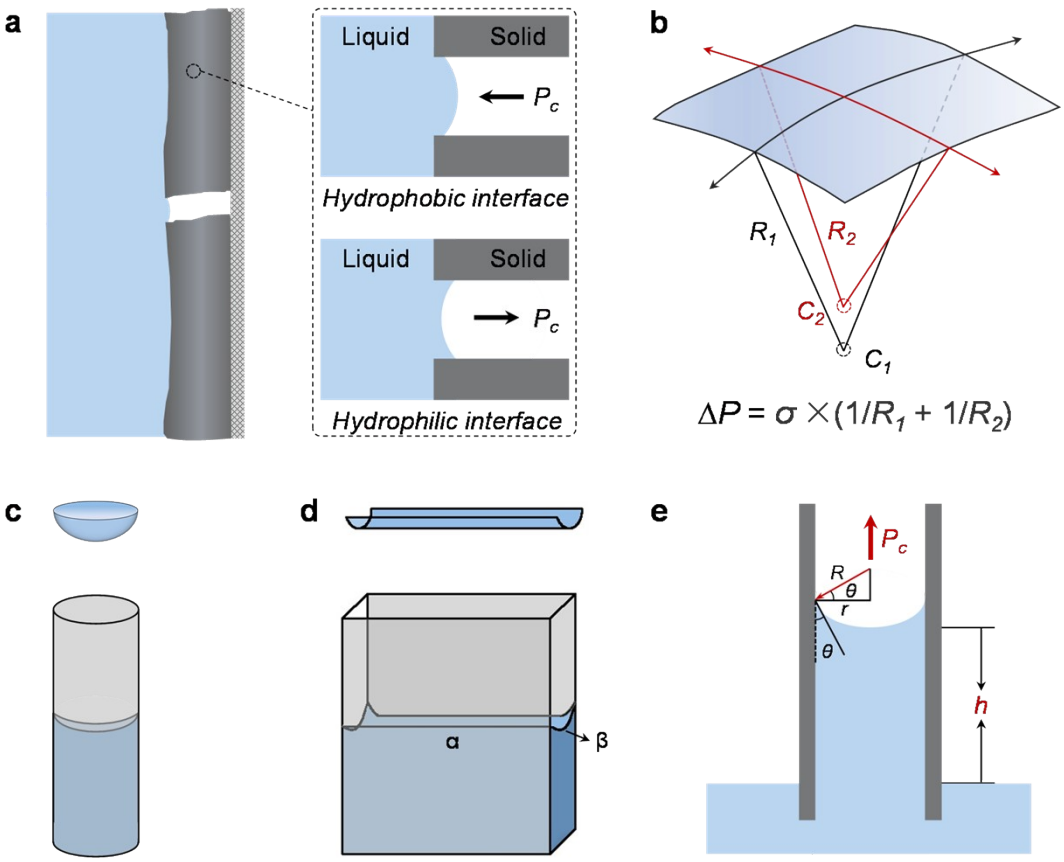

Fig. S27 Calculation model construction of capillary force-driven electrolyte infiltration into hydrophobic pores of electrodes. (a) Underwater DCP electrode model and analysis of pore wettability and capillary force direction. (b) The additional pressure on a curved liquid surface as a function of the radius of curvature. Schematic illustration of the dense and crack regions of the DCP electrode simplified into (c) cylindrical capillaries and (d) square capillaries. (e) Analysis of the rising height of the liquid column in a hydrophilic capillary.

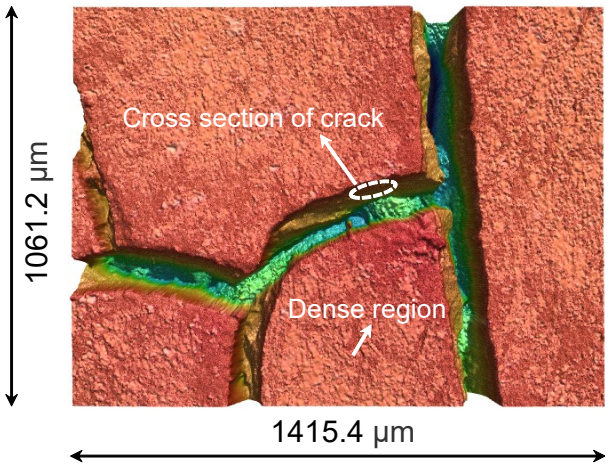

Fig. S28 Surface topography of DCP electrode obtained by 3D laser scanning microscopy. Location annotations corresponding to the scan results of "dense region" and "cross-sectional region of the crack" in the main text.

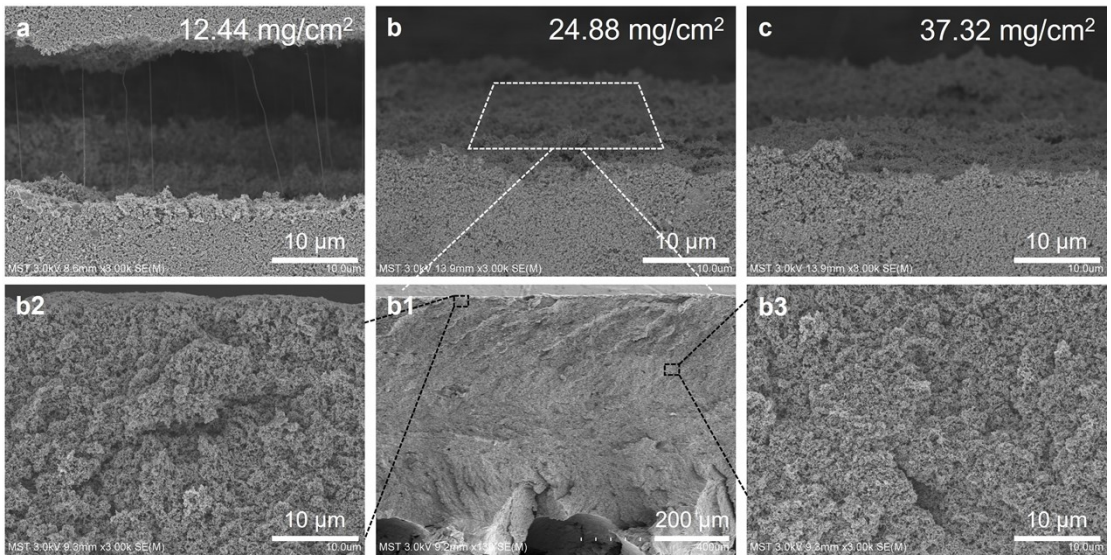

Fig. S29 Morphologies of the dense and crack regions of the DCP electrode. (a–c) SEM images of DCP electrodes with different CB loadings. (b1–b3) SEM images of the cross-section of the crack.

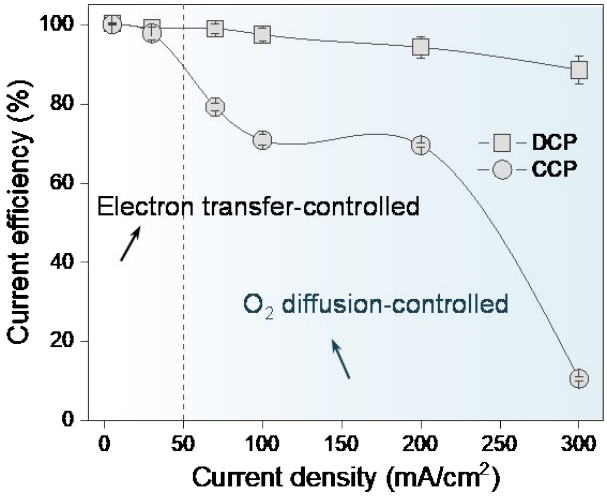

Fig. S30 H_2O_2 production performance of CCP and DCP electrodes. CE of CCP and DCP electrodes at different current densities in open air.

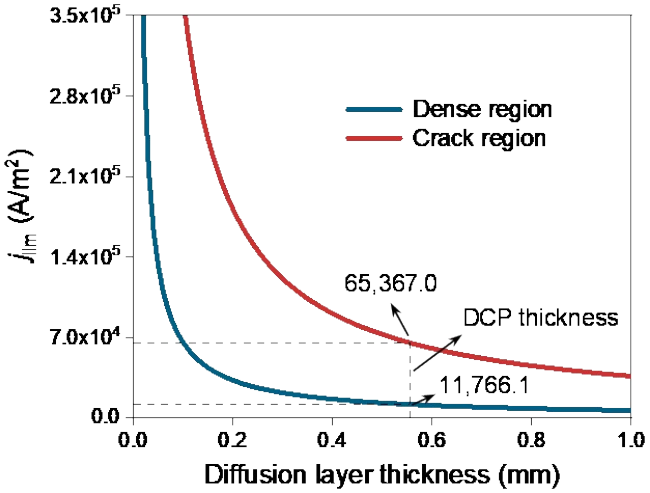

Fig. S31 Limiting current density for $2e^-$ ORR in different regions of the DCP electrode as a function of diffusion layer thickness.

When the mass transfer of air/O_2 inside the DCP electrode is the only rate-limiting step, the limiting current density (j_{lim}) of DCP for $2e^-$ ORR process in open air can be calculated according to equation: $j_{lim} = nFD_0C_0/\delta$,[14] where n is the number of electrons transferred for O_2 reduction to H_2O_2 (n = 2), F is the Faraday constant (96486 C/mol), D_0 is the diffusion coefficient of O_2 inside the DCP electrode (2.0×10^{-5} m^2/s for the crack region (equivalent to free diffusion in air)[17] and 3.6×10^{-6} m^2/s for the dense region[18]), C_0 is the concentration of O_2 in the air (9.4 mM), and δ is the diffusion layer thickness. We can then obtain the limiting current density in different regions of the DCP electrode as a function of the thickness of the O_2 diffusion layer, as shown in Fig. S31. If the three-phase equilibrium at the DCP-electrolyte interface is not destroyed (i.e., electrowetting), it can be assumed that the thickness of the O_2 diffusion layer is approximately the thickness of the DCP electrode (0.555 mm). Therefore, the limiting current densities of the dense region and crack region of the DCP electrode were calculated to be 1176.6 and 6536.7

mA/cm^2, respectively, which are both much higher than the highest current density value (500 mA/cm^2) we studied in this work. It is expected that the limiting current density of the electrode in open air can be further improved by reducing the electrode thickness and rationally optimizing the characteristics of the cracks. Our calculations suggest that air diffusion is sufficient to support stable operation of the DCP electrode at industrial-level current densities without the need for pure O_2 or air aeration.

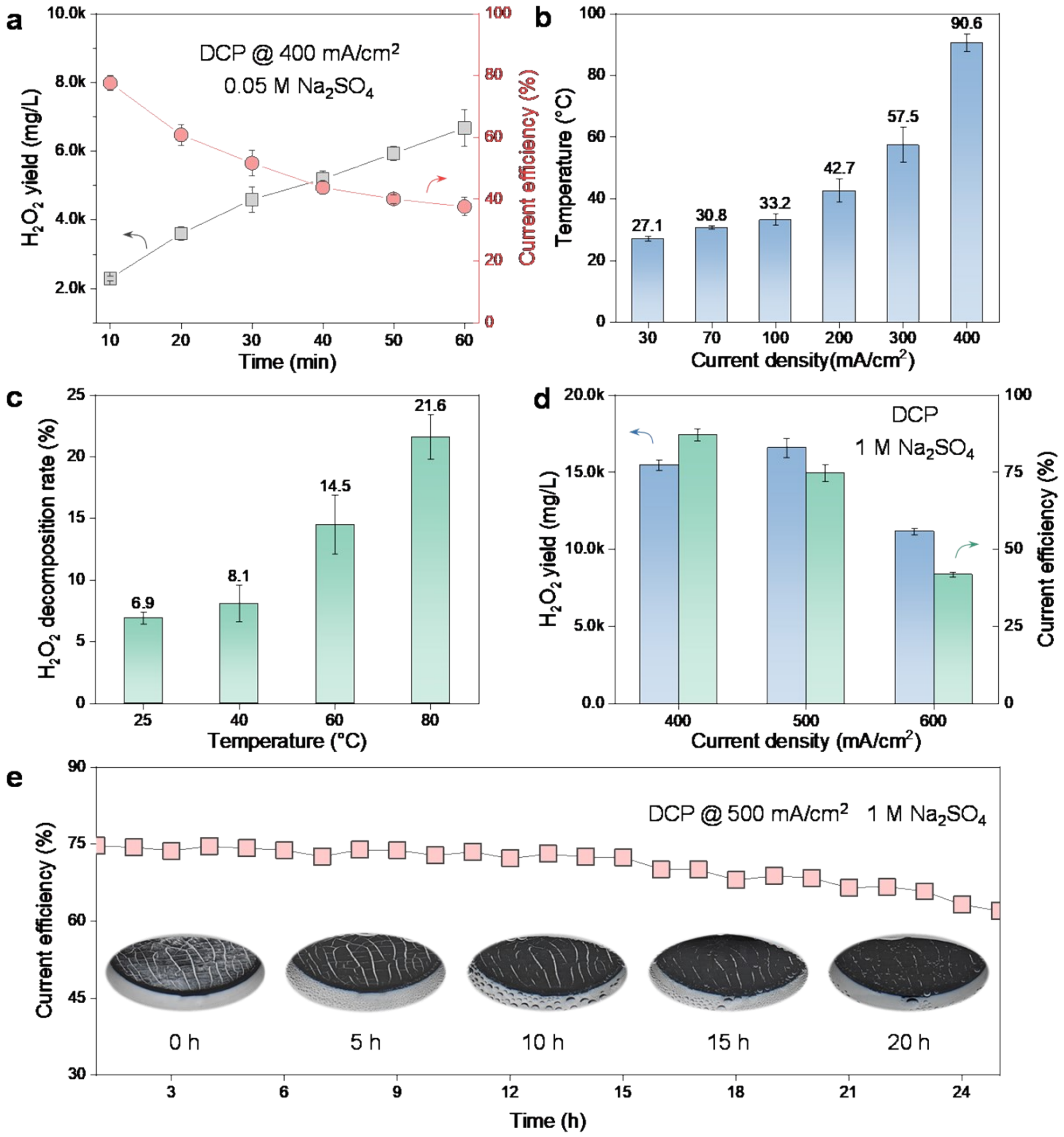

Fig. S32 Activity and stability of DCP electrode at current density >300 mA/cm^2. (a) H_2O_2 production performance of DCP in 0.05 M Na_2SO_4 at 400 mA/cm^2. (b) Temperature of 0.05 M Na_2SO_4 solution after 1 h of electrolysis at different current densities. (c) H_2O_2 decomposition rate at different electrolyte solution temperatures (conditions: [H_2O_2] = 1000 mg/L and 0.05 M Na_2SO_4). (d) H_2O_2 production performance of DCP in 1 M Na_2SO_4 at different current densities. (e) Catalytic stability of DCP in 1 M Na_2SO_4 at 500 mA/cm^2. Inset: wettability monitoring of the DCP electrode surface during a total reaction period of 25 h.

We further explored the performance of DCP at current densities higher than 300 mA/cm^2. Unfortunately, an undesirable drop in CE (<40%) was observed once the operating current density was increased to 400 mA/cm^2 (Fig. S32a). We consider that this decrease in CE is most likely related to the increase in temperature of the electrolyte solution. It is generally believed that H_2O_2 can undergo a spontaneous decomposition reaction in the bulk phase through the disproportion pathway ($2H_2O_2 \rightarrow O_2 + 2H_2O$), and its rate is largely determined by the solution temperature. For our experimental system, both the unoptimized electrolytic cell and the non-conductive PTFE binder in the DCP electrode can increase the internal resistance of the electrolytic system and thereby increase the temperature of the electrolyte through the promoted Joule heating effect. Indeed, we found that the temperature of the electrolyte solution increased significantly when the operating current density was greater than 100 mA/cm^2, even as high as 90.6 °C at 400 mA/cm^2 (Fig. S32b). We further monitored the decomposition kinetics of H_2O_2 with an initial concentration of 1000 ppm at different temperatures, and the results showed that the decomposition of H_2O_2 gradually accelerated as the temperature increased, especially above 60 °C (Fig. S32c). These facts indicate that the decreased CE of the DCP electrode at the operating current density of 400 mA/cm^2 is mainly attributed to the accelerated disproportionation decomposition of H_2O_2 in the electrolyte solution at 90.6 °C.

In order to alleviate this ineffective decomposition of H_2O_2, we increased the concentration of Na_2SO_4 from 0.05 M to 1 M, a concentration that is also frequently used in other $2e^-$ ORR or CO_2RR studies,[14,19,20] to reduce the internal resistance of the

electrolysis system. At this electrolyte concentration, the CE of DCP at 400 mA/cm^2 (87.1%, Fig. S32d) was observed to be significantly improved compared to that at 0.05 M (37.6%, Fig. S32a) due to the reduced cell voltage and solution temperature. Note that our DCP can still deliver a satisfactory CE of 74.7% even at 500 mA/cm^2, further illustrating the robust H_2O_2 production performance of this strategy. However, a decay in CE was again observed on DCP (41.9%, Fig. S32d) as the current density was further increased to 600 mA/cm^2, probably due to similar disproportionation decomposition effects as mentioned before. We also checked the durability of DCP in 1 M Na_2SO_4 at 500 mA/cm^2. The results in Fig. S32e show that the DCP electrode can operate stably for about 20 h, and the subsequent performance degradation may be because the high electrolyte concentration can accelerate the destruction of hydrophobicity at the crack by accelerating salt deposition at the electrode-electrolyte interface (inset of Fig. S32e). Note that although increasing the electrolyte concentration can further increase the operating current density of DCP, this approach may not be recommended. In addition to the detrimental effect in terms of electrode lifetime, more importantly, the presence of high concentrations of salt is undesirable for many distributed applications (such as environmental remediation), which would lead to the additional integration of energy-intensive and expensive H_2O_2 separation steps. Therefore, reducing the internal resistance and cell voltage by increasing the electrolyte concentration may not be advisable until the cost of the desalination procedure for H_2O_2 solutions is reduced to an industrially feasible threshold.

Continued research efforts in electrolysis device optimization or process coupling are recommended in the future.

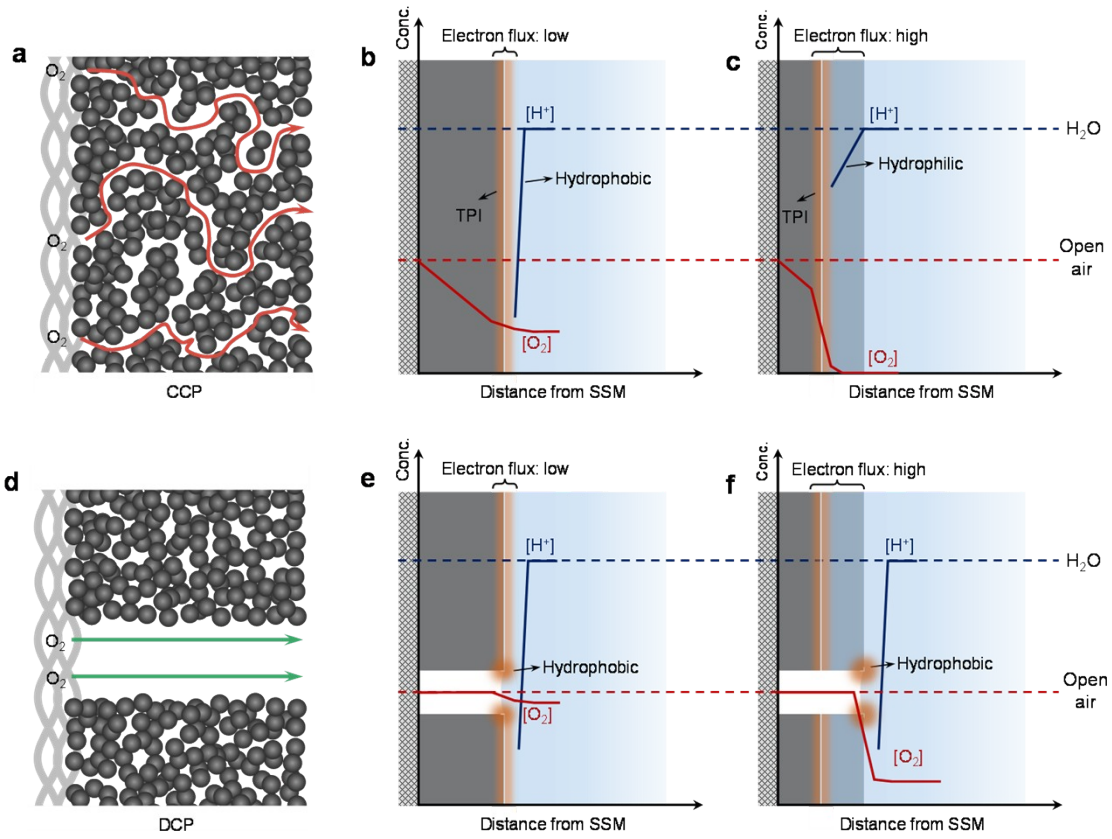

Fig. S33 Through-plane transport model of different reactants in the active layer of CCP and DCP during $2e^-$ ORR process. Schematic diagram of air transport through (a) CCP and (d) DCP electrodes. Concentration gradients of O_2 and protons in the active layer of CCP and DCP electrodes under (b, e) low and (c, f) high current density conditions. O_2 transports across the bulk structure of the electrodes towards the three-phase interface (TPI), while protons (i.e., H_2O) transport from the opposite electrolyte side to the TPI. The O_2 consumption rate within the TPI layer is significantly higher at high current densities than at low current densities, which is represented by the higher slope of the red line within the TPI layer. Note here that for the convenience of demonstration, the initial concentrations of H_2O and O_2 were set at the same order of magnitude, but in fact the concentration of H_2O is much higher than that of O_2.

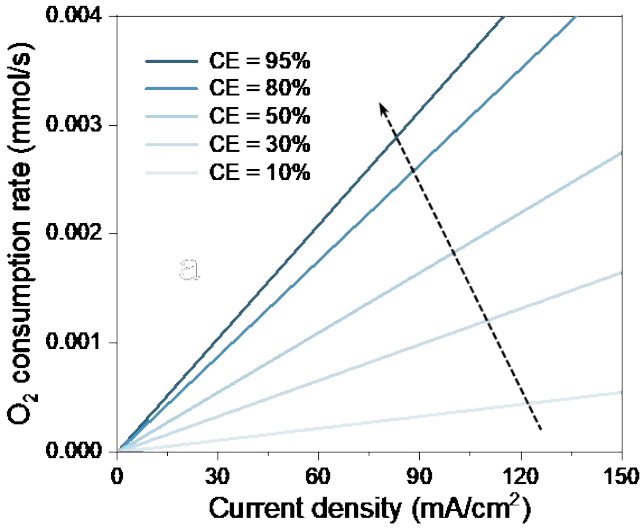

Fig. S34 O_2 consumption rate at the reaction interface as a function of operating current density at different CE. The consumption rate of O_2 (r, mmol/s) at the reaction interface can be calculated by using the Faraday electrolysis law: $r = j\eta S/nF$, where j is the current density (mA/cm^2), η is the CE for H_2O_2 production (%), S is the electrode effective area (cm^2), n is the number of electrons transferred for O_2 reduction to H_2O_2 (n = 2), and F is the Faraday constant (96486 C/mol).

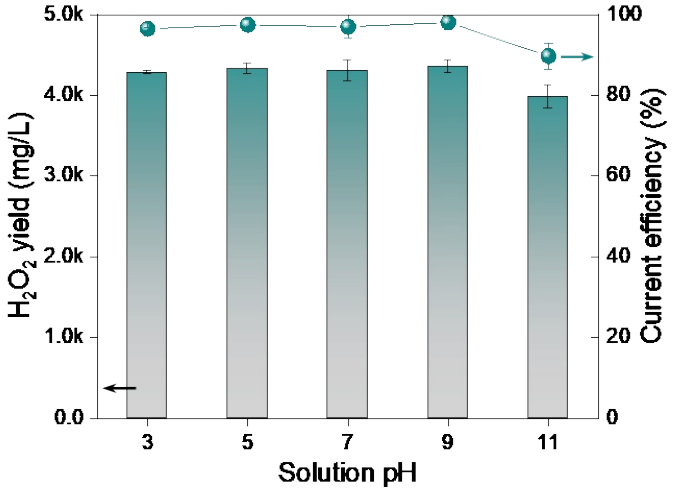

Fig. S35 Tolerance test of the DCP electrode to electrolyte pH. H_2O_2 production performance of the DCP electrode at different electrolyte pH values.

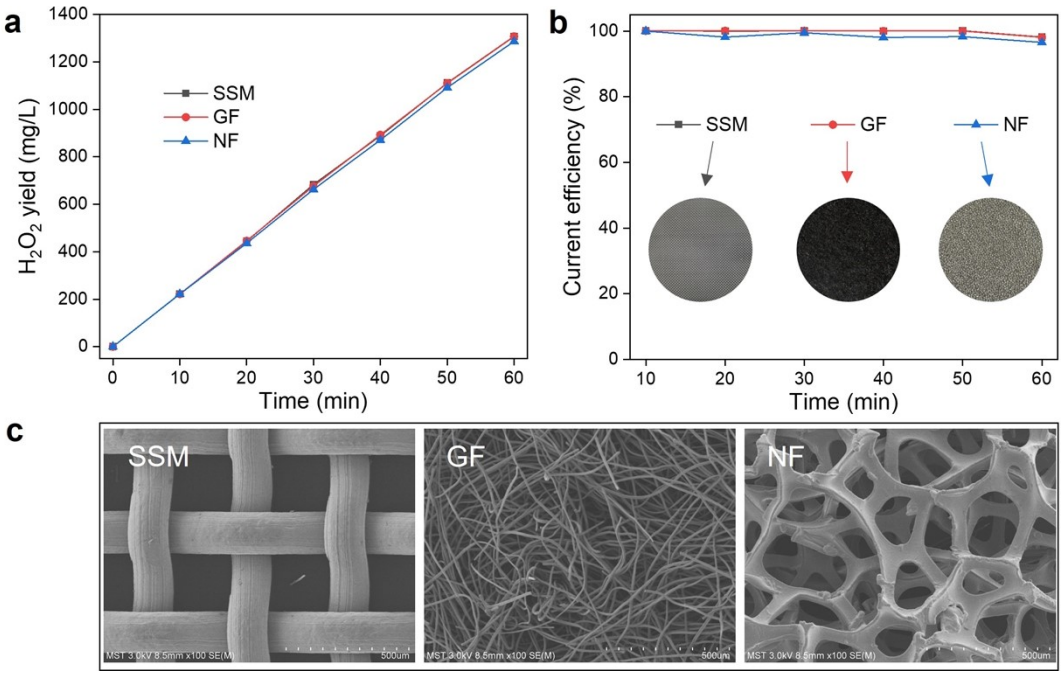

Fig. S36 Generality of the concept of anti-electrowetting carbon film electrode with self-sustained aeration to electrode matrix materials. (a) H_2O_2 yield and (b) CE of DCP electrodes supported by SSM, GF and NF. Inset in (b) shows photos of different supports. (c) SEM images of SSM, GF and NF substrates.

We found that this concept of anti-electrowetting carbon film electrode with self-sustained aeration has broad applicability to different substrates. CB-PTFE films supported by SSM, GF, or NF all exhibit excellent H_2O_2 production performance with a CE close to 100%. We suggest that different substrates can be selected according to different purposes and scenarios. For example, for laboratory experiments aimed at proof of concept, flat and rigid substrates such as SSM can be utilized. While for scale-up systems that require long service lifespan, the substrates with a complex pore structure treated with PTFE for better water resistance, such as GF and NF, may be more suitable. Note that GF and NF have their own advantages. For example, the conductivity of GF is better than NF, but the loading of the catalytic film on NF is

more convenient and stable than GF due to its high mechanical strength and regular surface. It is necessary to state that it is the NF-supported DCP electrode that we utilized in our 12 L pre-pilot scale tests.

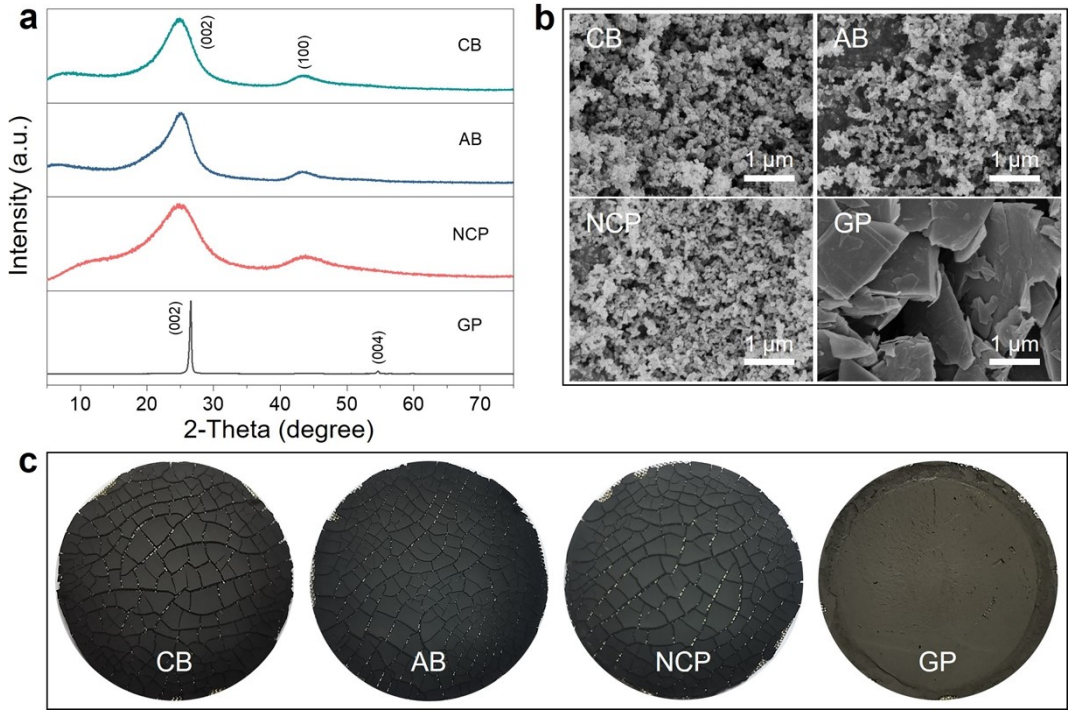

Fig. S37 Characterization of different carbon electrocatalysts. (a) XRD patterns and (b) SEM images of CB (carbon black), AB (acetylene black), NCP (nano-carbon powder) and GP (graphite powder). (c) Photos of discontinuous electrodes made from CB, AB, NCP, and GP.

According to the morphology observations of different carbon electrocatalysts, it seems feasible to form cracks in the nanoparticle coating whereas it is apparently difficult for graphite probably due to its layered structure.

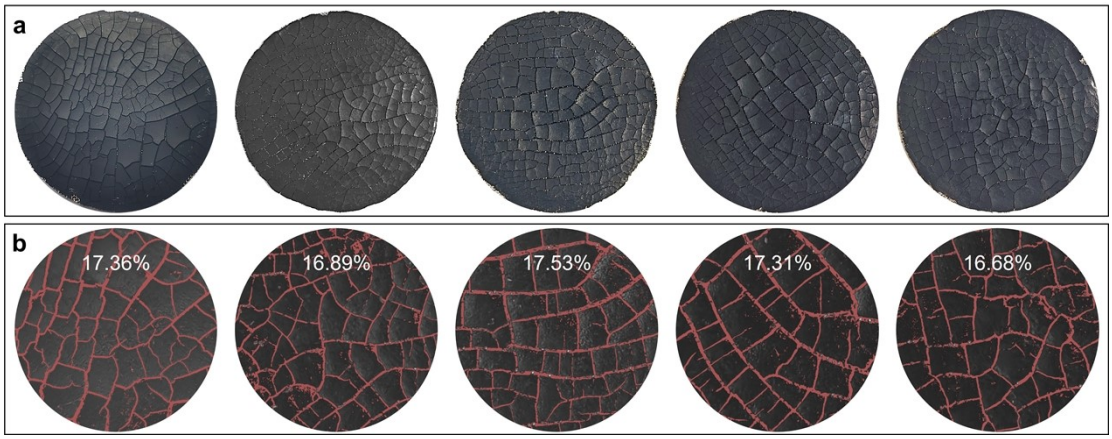

Fig. S38 Repeatability of DCP electrodes. (a) Optical images and (b) crack density of different batches of DCP electrodes fabricated in different periods.

Benefiting from the simplification and convenience of the procedures involved in the coating-calcination method proposed in this work, the fabricated DCP electrodes are highly stable and repeatable in structure. Specifically, as long as important variables such as CB loading, drying temperature, and calcination temperature are well controlled, the crack density of different batches of DCP electrodes manufactured in different periods is almost unchanged. This is also a key prerequisite that enabled us to easily scale up the DCP electrode and achieve its stable operation at practical production rates in industrial electrolyzers.

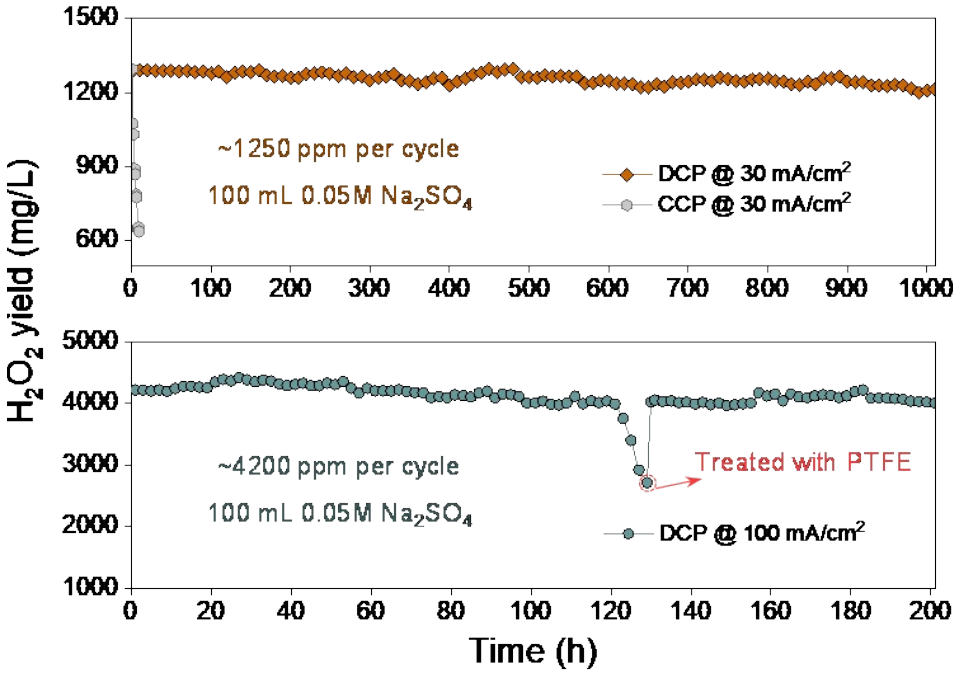

Fig. S39 Electrode durability test. H_2O_2 yield (mg/L) per cycle (1 h) for CCP and DCP electrodes operating continuously at 30 mA/cm^2 (100 mA/cm^2) for 1000 h (200 h).

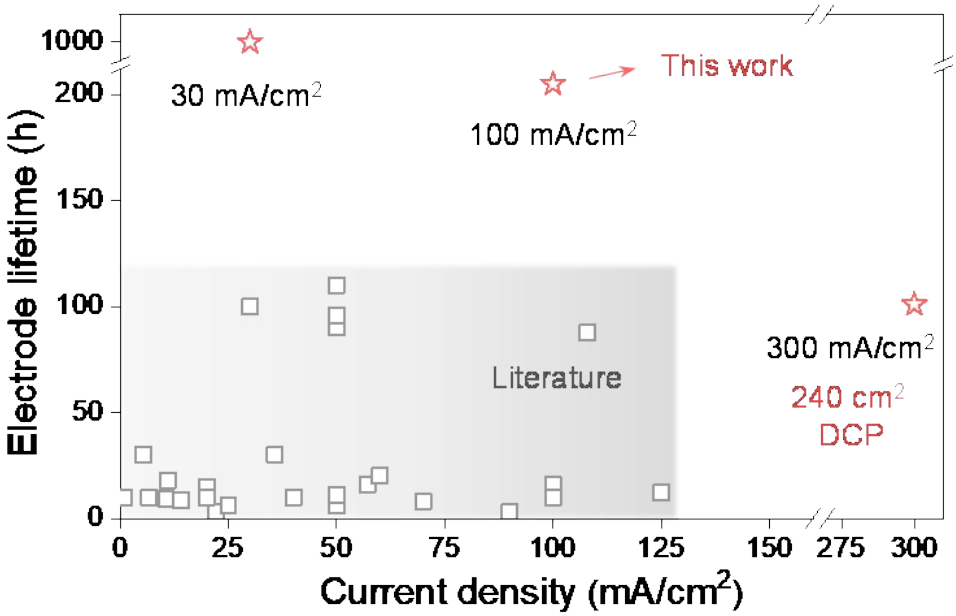

Fig. S40 Comparison of crack-enhanced strategy with recent literature on the topic of H_2O_2 electrosynthesis in terms of electrode lifetime (Table S1).

Under routine laboratory-level current density test conditions (30 mA/cm^2), the lifespan of the DCP electrode can exceed 1000 h, which is about an order of magnitude higher than the value reported in the literature. Even at extremely challenging industrially relevant current density of 100 mA/cm^2 (300 mA/cm^2), the DCP electrode delivered an unprecedented durability of more than 200 h (100 h). More attractively, the DCP electrode operates without any external aeration equipment, demonstrating significant economic and operational advantages over GDE or membrane electrode assembly devices generally relying on compressed oxygen or air pumps in the literature.

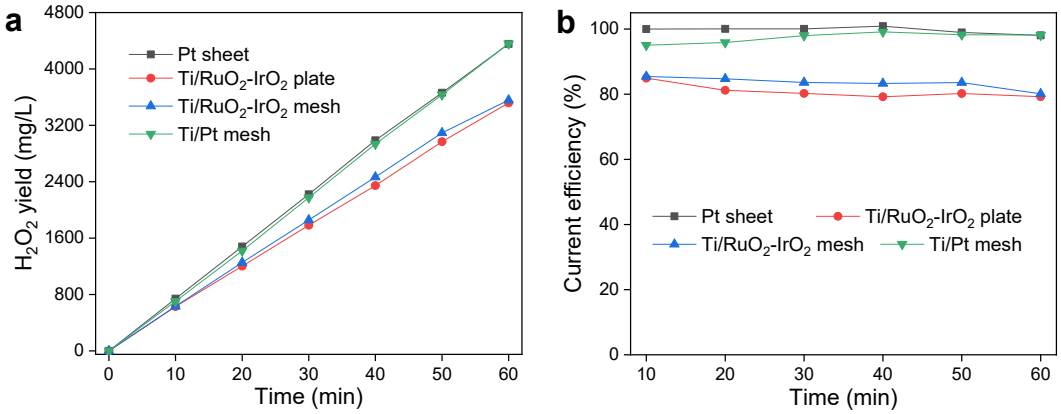

Fig. S41 Selection of anode material. (a) H_2O_2 yield and (b) CE of different anodes with DCP as cathode.

It is well known that H_2O_2 produced at the cathode is likely to be oxidatively decomposed at the anode in typical undivided electrolyzers,[1] and this effect is expected to be exacerbated in scale-up setups due to the larger anode area. In order to minimize this effect and reduce the cost of materials, we screened several industrial anodes and conducted comparative experiments on H_2O_2 electrosynthesis. The results in Fig. S41 show that the Ti/RuO_2-IrO_2 plate and Ti/RuO_2-IrO_2 mesh anode did cause the ineffective decomposition of H_2O_2 in the system, while the Ti/Pt mesh anode system exhibited comparable H_2O_2 yield and CE to the Pt sheet anode. More critically, the market cost of Ti/Pt mesh is less than one-tenth of Pt sheet, so we finally select Ti/Pt mesh as the anode material in the scaled-up device.

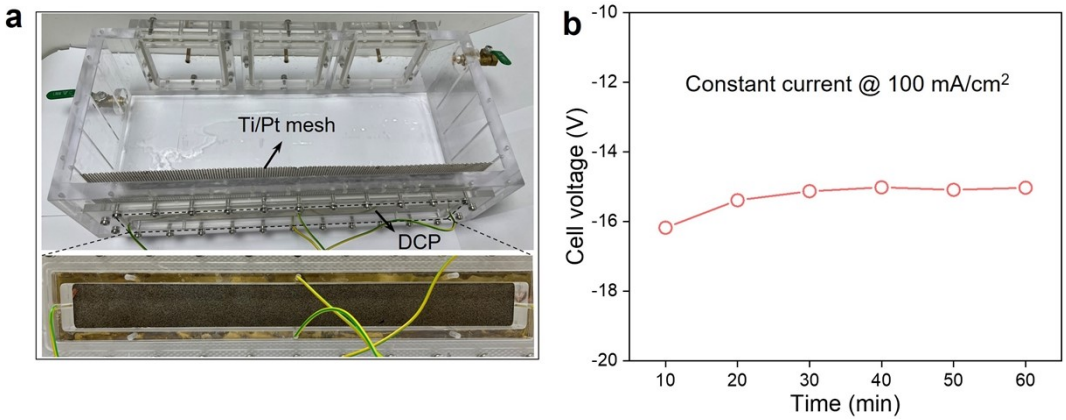

Fig. S42 Scale-up of the anti-electrowetting carbon film electrode with self-sustained aeration. (a) Optical image of the scale-up DCP electrode (240 cm^2, 40 cm × 6 cm) and the supporting electrolyzer. (b) Cell voltage curves over reaction time in this system.

The cost-effective and convenient DCP electrode preparation process allows it to be easily scaled up to 240 cm^2, and the electrolytic cell can also be easily scaled up to a fit-for-purpose industrially relevant scale. Encouragingly, we did not find significant amplification effects in our 12 L device with CE still exceeding 90% (Fig. 5(g) in the main text). An unprecedented 12 L of H_2O_2 solution with a concentration of ~1200 ppm can be stably (cell voltage) produced in just one hour.

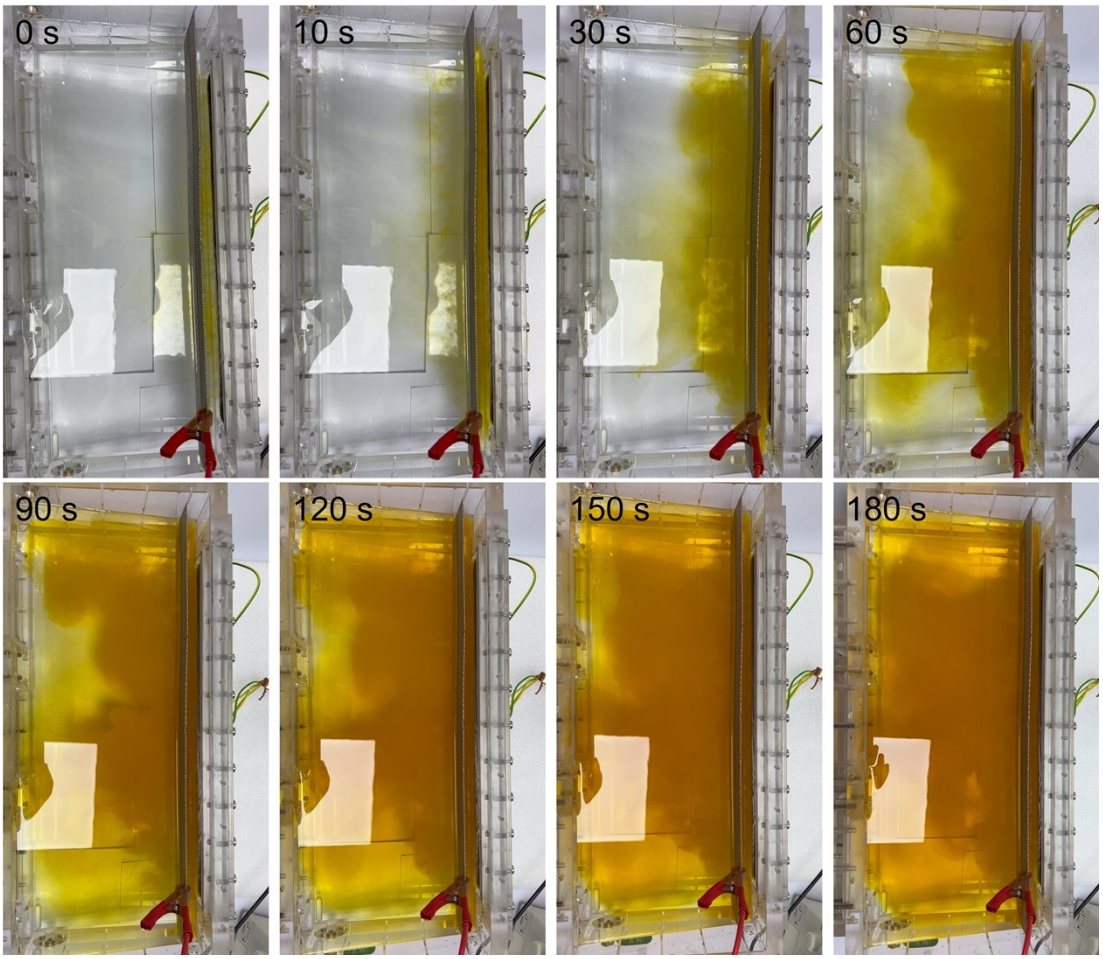

Fig. S43 Visualization of the H_2O_2 production process by the DCP cathode in the scaled-up system.

Before initiating the reaction, 100 mL of potassium titanium (IV) oxalate was added to the reactor, serving as a chromogenic agent for H_2O_2. It has previously been exhibited that potassium titanium (IV) oxalate reacts with H_2O_2 to form a stable yellow-orange titanium (IV)-peroxide complex, with its color depth being proportional to the concentration of H_2O_2.[21] Therefore, the H_2O_2 production process can be visualized in real time under static conditions through chromogenic observations. The rapid transition of the electrolyte color from colorless to orange in Fig. S43 demonstrates the excellent H_2O_2 production performance of our scaled-up DCP system.

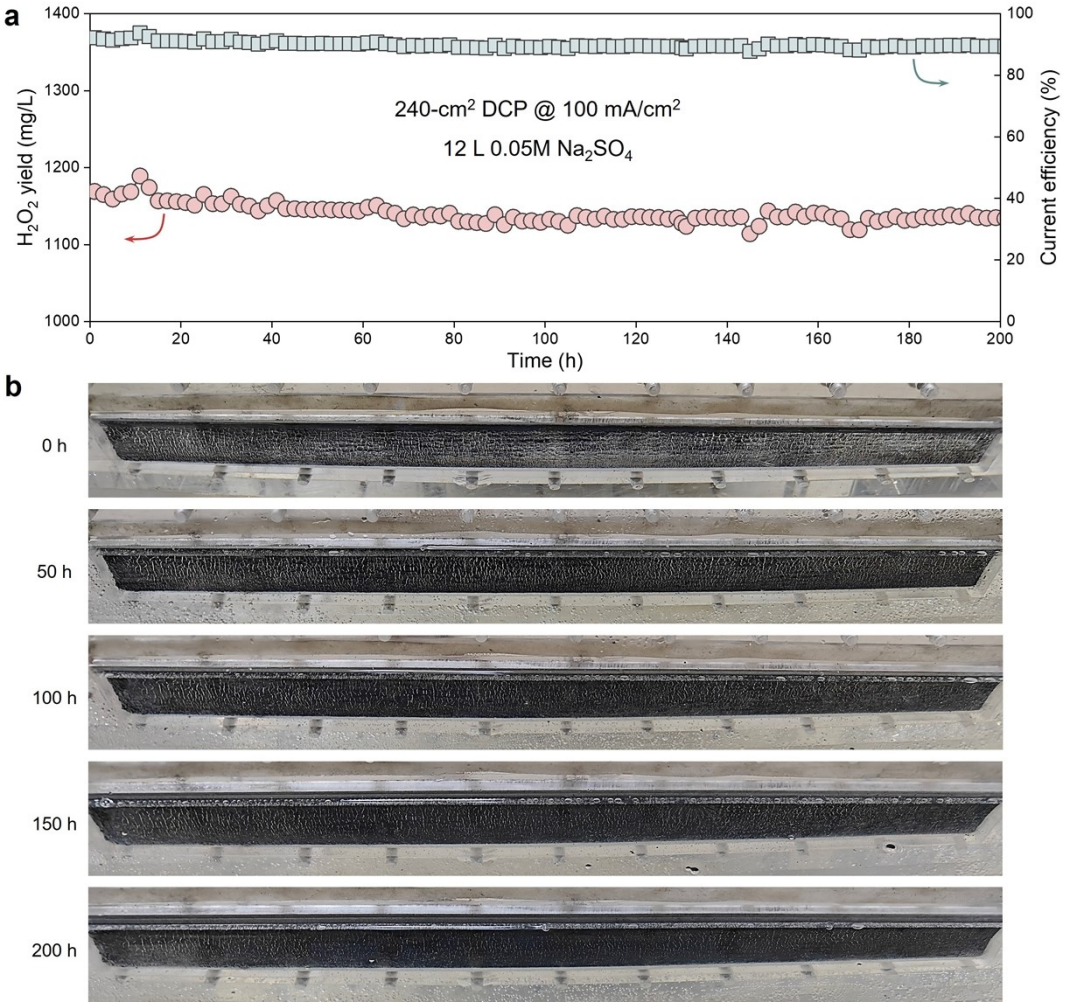

Fig. S44 Durability test of the 240-cm^2 DCP electrode. (a) H_2O_2 yield (mg/L) and CE (%) per cycle (1 h) for DCP operating continuously at 100 mA/cm^2 for 200 h. (b) Wettability monitoring of the DCP electrode surface during the total reaction period of 200 h.

It should be noted that the stability test of the bench-scale DCP in the main text was performed using a Pt foil counter electrode with a working area (1 cm^2) much smaller than that of the DCP electrode (7 cm^2). This configuration may increase the internal resistance and the cell voltage of the electrolysis system, especially at an operating current density of 100 mA/cm^2. For our 12-L pre-pilot scale plant, however, a substantial reduction in cell voltage (from ~24 V to ~15 V, Fig. S42b) was observed

due to the deployment of inexpensive platinum-coated titanium mesh anode with a geometric area comparable to that of the 240-cm^2 DCP. As a result, the 240-cm^2 DCP electrode can operate stably for more than 200 h at an operating current density of 100 mA/cm^2 (>90% CE, Fig. S44a) without cracks being completely flooded (Fig. S44b), which is different from the 100-mL electrolyzer that requires additional PTFE treatment of 7-cm^2 DCP after 130 h (Fig. 5(e) of the main text).

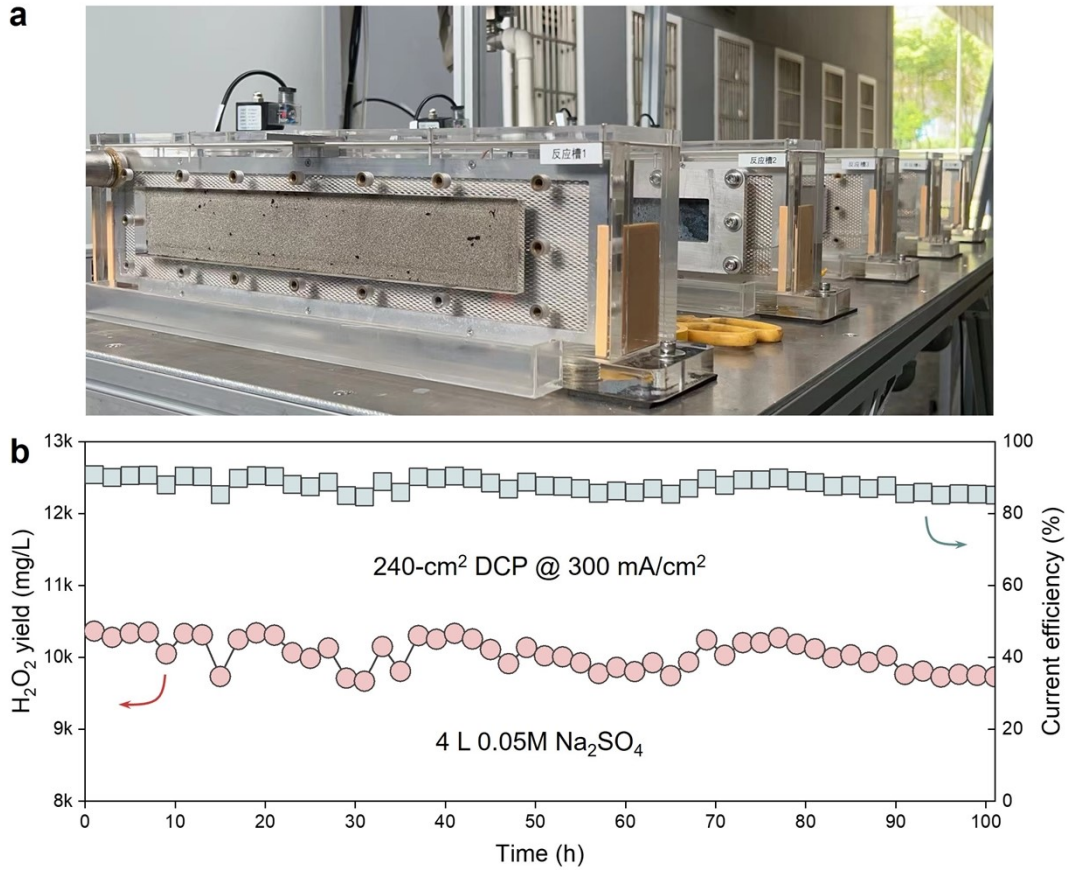

Fig. S45 Durability test of the 240-cm^2 DCP electrode. (a) Optical image of a membrane-free flow cell. (b) H_2O_2 yield (mg/L) and CE (%) per cycle (1 h) for DCP operating continuously at 300 mA/cm^2 for 100 h.

We further demonstrate the catalytic stability of the scale-up DCP at a higher current density of 300 mA/cm^2. Considering that neither the output current threshold of the laboratory-scale DC power supply nor the current-carrying capacity of the wires could meet the required high current of 72 A, we no longer performed this experiment in this pre-pilot scale plant. Instead, we performed this experiment in a compact membrane-free flow cell (co-developed with Shuangliang Environmental Technology Co., Ltd) equipped with 240-cm^2 DCP electrodes (Fig. S45a). This compact assembly strategy can further reduce the cell voltage due to accelerated overall mass transfer and shortened interelectrode distance. As a result, the 240-cm^2

DCP electrode can even operate stably at a current density of 300 mA/cm^2 for more than 100 h (Fig. S45b), strongly demonstrating the industrial feasibility of our proposed electrode crack engineering strategy. Note that 4 L of >1.0 wt% H_2O_2 solution produced per hour can be directly used in distributed wastewater treatment scenarios.

Table S1. Comparison of H_2O_2 production performance among various modification strategies presented in Fig. 5(c) of the main text.

Strategy	Cathode	Catalyst	Electrolyte	Current density (mA/cm^2)	O_2 source	H_2O_2 yield ($mg/cm^2/h$)	CE	Service life	Ref.
SAE modification	GF	O/F co-doped CNTs	0.05 M Na_2SO_4	20	−	9.29	73.1%	15 h	22
	ACF	g-C_3N_4/CNTs	0.05 M Na_2SO_4	6.67	Air aeration	3.96	~45%	10 h	23
	GF	CB	0.05 M Na_2SO_4	11	O_2 aeration	5.28	~65%	18 h	24
	NGC	−	0.05 M Na_2SO_4	1	O_2 aeration	0.07	−	10 h	25
	GF	−	0.05 M Na_2SO_4	5.32	O_2 aeration	2.77	75.7%	30 h	26
Electrocatalyst design	GDE	NPC	1 M KOH	100	O_2 aeration	58.00	97%	200 h	20
	GDE	Co−N−C	0.1 M KOH	50	O_2 aeration	14.72	~46%	6 h	27
	GDE	CoS_xP_y/ MWCNTs	0.05 M Na_2SO_4	40	Air aeration	4.51	54%	−	28
	GDE	CNT/NCB	0.2 M Na_2SO_4	57.14	Air aeration	8.43	50.25%	16 h	29
	GDE	CoSP/ MWCNTs	0.05 M Na_2SO_4	25	Air aeration	3.63	52.6%	−	30
	ABC	TRGO	0.05 M Na_2SO_4	40	Open air	20.61	81%	10 h	31
	GDE	CNT	0.05 M Na_2SO_4	10.7	Air aeration	5.1	75%	9 h	32
	GDE	CNT	0.05 M Na_2SO_4	31.85	Air aeration	17.6	70%	−	33
	NADE	In SAs/NSBC	0.1 M Na_2SO_4	90	Open air	44.13	77.34%	3 h	34
	GDE	PtP_2	0.1M $HClO_4$	150	O_2 aeration	76.84	78.8%	−	35
	GDE	COF-366-Co	0.1 M KOH	22	Open air	10.82	82%	3 h	36
	CP	Co_1–NG(O)	0.1 M KOH	50	O_2 aeration	14.21	−	110 h	37
	GDE	O-CNTs	1 M KOH	20	O_2 aeration	1.90	−	10 h	38
	GDE	Ni-N_2O_2/ C	0.1 M KOH	70	Air/O_2 aeration	40.12	90%	8 h	39
	GDE	Graphene	0.1 M KOH	100	O_2 aeration	60.7	94%	16 h	40
	GDE	NiB_2	0.1 M KOH	125	O_2 aeration	64.64	~93%	12 h	41

	GDE	Co−N SAC	0.1 M $HClO_4$	50	O_2 aeration	26.7	84%	90 h	42
	GDE	$OCNS_{900}$	0.1 M KOH	50	O_2 aeration	26.18	82.5%	11 h	43
System optimization	Floating GF/RVC	–	0.05 M Na_2SO_4	16.67	Open air	2.22	21%	–	44
	GDE	AB	0.3 M Na_2SO_4	20	O_2 aeration	8.46	~35%	–	45
	GDE	CB	0.05 M Na_2SO_4	35.7	Air aeration	12.16	51%	30 h	46
	ABC	CB	0.05 M Na_2SO_4	35	Open air	13.59	61%	–	47
	ABC	CB&G	0.05 M Na_2SO_4	25	Open air	12.02	76%	6 h	48
	GF	–	0.05 M Na_2SO_4	8.82	O_2 aeration	1.94	67%	–	49
	PBs	–	0.05 M Na_2SO_4	14.1	O_2 aeration	4.79	53.9%	8.3 h	50
	CB/PTFE/ Ti mesh	CB	0.05 M Na_2SO_4	5	O_2 aeration	2.15	~67%	–	51
	GDE	CB	Solid electrolyte	50	Air aeration	20.3	58.4%	96 h	52
	NADE	CB	0.05 M Na_2SO_4	20	Open air	10.97	86.5%	–	53
				60		30.93	81.8%	20 h	
				240		101.67	66.8%	–	
	ABC	CB	0.05 M Na_2SO_4	30	Open air	16.13	84%	–	54
	GDE	CB	Solid electrolyte	30	O_2 aeration	18.02	95%	100 h	55
				200		115.6	90%	–	
	ABC	O-BC	0.05 M Na_2SO_4	100	Open air	40.7	64.2%	10 h	56
	GDE	AB	0.05 M Na_2SO_4	108	Air aeration	54.2	79.1%	87.5 h	57
Crack-mediated	DCP	CB	0.05 M Na_2SO_4	5	Open air	3.18	100%	–	This work
				30		18.89	99.30%	>1000 h	
				100		61.87	97.54%	>200 h	
				200		119.68	94.34%	–	
				300		168.64	88.62%	>100 h	
			1 M Na_2SO_4	400		220.99	87.11%	–	
				500		236.91	74.70%	~20 h	

SAE: submerged aeration electrode; GF: graphite felt; CNTs: carbon nanotubes; ACF: active carbon fiber; CB: carbon black; NGC: nitrogen-enriched graphitic carbon;

GDE: gas diffusion electrode; NPC: N-doped carbon; Co−N−C: N-doped carbon materials featuring atomically dispersed Co cations; CoS_xP_y/MWCNTs: (Co, S, P)-decorated multiwalled carbon nanotubes; NCB: N-doped carbon black; ABC: air breathing cathode; TRGO: thermal reduced graphene oxide; In SAs/NSBC: In single atoms anchored by combined N,S-dual first coordination and B second coordination supported by the hollow carbon rods; COF-366-Co: covalent organic framework-based Co catalysts; CP: carbon paper; Co_1–NG(O): Co–N_4 moiety incorporated in nitrogen-doped graphene; O-CNTs: oxidized carbon nanotubes; Ni-N_2O_2/C: carbon-supported Ni centers coordinated by two O atoms and two N atoms; SAC: single-atom catalyst; $OCNS_{900}$: oxygen-doped carbon nanosheet; RVC: reticulated vitreous carbon; AB: acetylene black; CB&G: carbon black/graphite; PBs: pine blocks; NADE: natural air diffusion electrode; O-BC: O-doped biochar.

Text S1. Discussion of $2e^-/4e^-$ ORR selectivity in realistic electrode operation.

It is generally believed that the H_2O_2 production performance in the device is mainly determined by the selectivity of the electrocatalyst. Interestingly, it has been demonstrated in many literature that even the simplest materials, especially CB, can have excellent selectivity for H_2O_2 formation provided the reaction is driven at moderate current densities.[19,58–61] For example, Zhang et al. introduced the cation effect (specifically, the shielding effect of cations on local protons), which has been well understood in the field of CO_2RR, into the $2e^-$ ORR process and thereby achieved a stable H_2O_2 production process with a current efficiency of ~90% at 50 mA/cm^2 in strong acid media using just commercial CB.[58] It can therefore be considered that even for pristine CB its intrinsic selectivity is actually acceptable for on-site production of H_2O_2. Note that in the preparation of our CCP/DCP electrode the CB underwent a co-calcining process with PTFE (very common for electrode preparation processes using PTFE as a binder), during which the surface of the CB may be functionalized with heteroatom fluorine. The XPS results (Fig. S46a) show the presence of oxygen-containing functional groups on the surface of the DCP electrode, along with the appearance of a new peak that can be assigned to covalently bonded CF_2. The generation of CF_2 is expected to further improve the $2e^-$ ORR selectivity of pristine CB due to the moderate *OOH binding energy at the CF_2-associated site, which has been rigorously demonstrated in several previous studies involving heteroatom-modified carbon electrocatalysts for H_2O_2 production.[19,62] As further evidence, we additionally performed RRDE analysis and the results showed

that the CB peeled from the DCP structure indeed exhibited nearly 80% H_2O_2 selectivity (Fig. S46b−d), which is an important origin of the excellent O_2-to-H_2O_2 conversion efficiency at the crack edge of our DCP electrode.

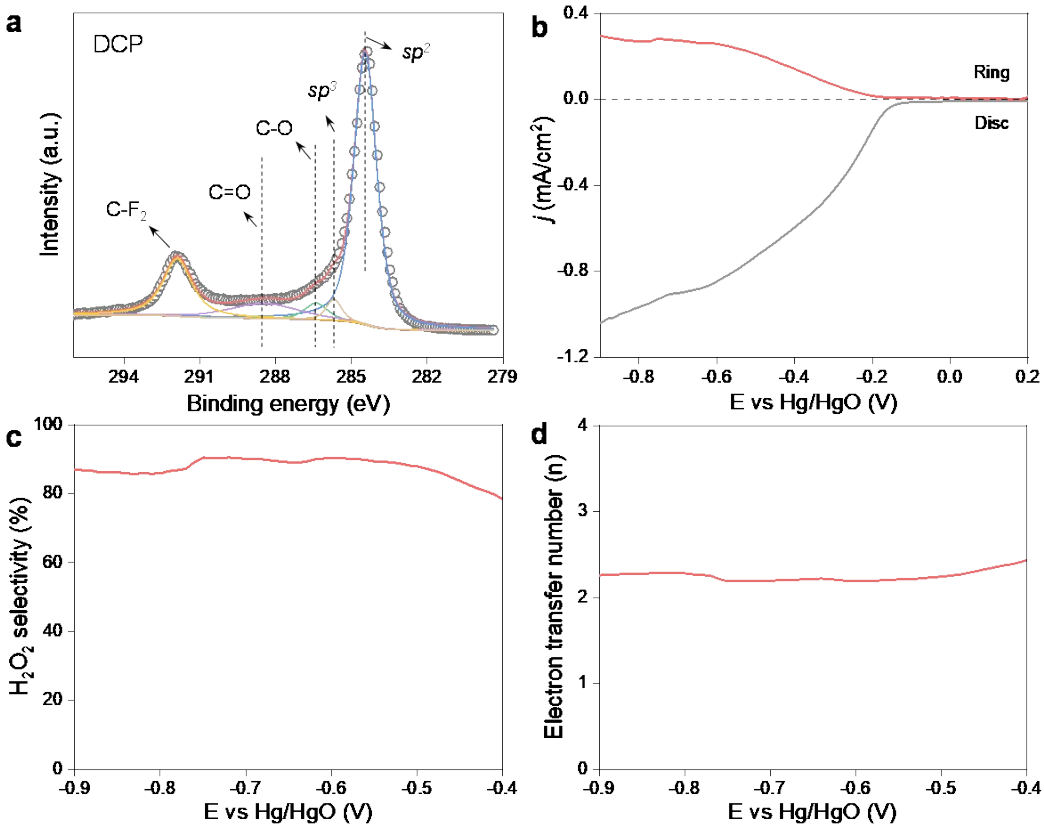

Fig. S46 (a) High-resolution C 1*s* XPS spectrum of DCP electrode. (b) RRDE test of CB in DCP structure and the corresponding (c) H_2O_2 selectivity and (d) electron transfer number.

Regarding the contradiction between the H_2O_2 selectivity value (~80%) of CB obtained in the RRDE test and the H_2O_2 production current efficiency value (~100%) of the DCP electrode obtained in the device test, in fact this phenomenon is common and can be found in many previous studies.[19,20,58,59,63] Taking a recent report as an example,[19] although the heteroatom-doped (O or F) CB electrocatalyst exhibited a H_2O_2 selectivity of ~80% in the RRDE test, it still achieved nearly 100% Faradaic

current efficiency at 0.55−0.75 V vs RHE in the flow cell test. Unfortunately, however, the fundamental understanding of this phenomenon is hitherto lacking, probably due to the multitude of cross-scale processes occurring in three-dimensional GDE and the complex interactions between them (completely different from the almost idealized testing conditions of RRDE). We currently propose to rationalize this phenomenon from the perspective of microenvironmental tuning at the electrode interface. First, the importance of the microenvironment in gas-involving electrocatalytic reactions can be emphasized through a simple analysis of the relationship between reactant ratio and product selectivity. For our research system, three key reactions occur at the active interface of the cathode, namely $2e^-$ ORR ($2O_2 + 4H^+ + 4e^- \rightarrow 2H_2O_2$), $4e^-$ ORR ($O_2 + 4H^+ + 4e^- \rightarrow 2H_2O$) and hydrogen evolution reaction (HER) ($0O_2 + 4H^+ + 4e^- \rightarrow 2H_2$). Under the premise of the same Faraday electron consumption, the demand for O_2 in the three reactions increases in the following order: HER < $4e^-$ ORR < $2e^-$ ORR (that is why we defined HER as "non-O_2-demand" and $4e^-$ ORR as "low-O_2-demand" in the main text). It can therefore be estimated that the H_2O_2 production is extremely sensitive to the O_2 content at the active site, which is essentially determined by the O_2 capture capability controlled by the surface properties of the electrode. Once O_2 accessibility to the cathode interface is destroyed, the resulting O_2 starvation in the microenvironment is expected to immediately switch the process selectivity toward the low-O_2-demand $4e^-$ ORR or even non-O_2-demand HER. Therefore, it can be considered that for those electrocatalysts with moderate intrinsic $2e^-$ selectivity (such as the CB we used), a

suitable microenvironment (i.e., constant sufficient O_2 supply) at the electrode interface may play a governing effect in modulating the reaction selectivity for H_2O_2 production, especially under high current density conditions where O_2 demand increases dramatically. Our DCP electrode provides a stable aerophilic microenvironment at the crack edge due to its robust anti-electrowetting effect, which is apparently able to promote the preferential generation of H_2O_2 according to the aforementioned effects. Similar phenomena of controlling product selectivity by changing the interfacial wettability and microenvironment (rather than the intrinsic selectivity of the electrocatalyst) of GDE electrodes have also been reported in the field of CO_2RR.[64]

In addition to mass transfer optimization of oxygen reactants, microenvironmental modulation may also be reflected in local pH changes on the electrode surface. For ORR, a highly proton-consuming reaction, the surface of the working electrode is expected to undergo rapid local alkalinization that is completely different from the pH stabilization of the bulk solution. To date, research on the benefits of local alkalinity phenomena at the GDE interface is arguably quite extensive in the field of CO_2RR.[65–67] Specifically, the local alkaline microenvironment can effectively stabilize the adsorbed OCCO intermediate through the enhanced dipole attraction within OCCO (or the increased charge imbalance between carbon atoms in OCCO), thereby significantly promoting the selective conversion of CO_2 into C_2 products. This principle is likely to be applicable to our $2e^-$ ORR process considering the similar structures of the HOOH intermediate (the intermediate before H_2O_2 desorption from

the active site) and the OCCO intermediate. Once this conjecture is established, the local alkalinity at the electrode interface may be extremely critical for the H_2O_2 production process, because it affects the preference of HOOH intermediates for safe desorption or over reduction to H_2O. In fact, a similar phenomenon of stabilizing reaction intermediates through local pH elevation on the electrode surface has recently been preliminarily verified in a $2e^-$ ORR study.[59] For our DCP electrode, the stable hydrophobicity at the crack edge may induce faster local alkalinization than the dense region due to restricted diffusion of water molecules at the hydrophobic interface.[68] Therefore, we speculate that the reaction intermediates at the crack edge of the DCP electrode are likely to be stabilized due to rapid alkalization here, which is conducive to the selective generation of H_2O_2. Of course, sufficient and rigorous experimental design and theoretical calculations are urgently needed to support the above discussion about local alkalization phenomenon. This is indeed a research project that we are highly concerned about and have been ongoing recently. In summary, combining the above discussions and the experimental phenomena observed in the main text, it seems possible to conclude that the characteristics of the microenvironment at the electrode interface (such as wettability and local pH, etc.) and the intrinsic selectivity of the electrocatalyst can interplay to determine the current efficiency of H_2O_2 production in realistic electrode operation.

Text S2. Calculation of O_2 pressure difference between reaction interface and surrounding air.

First, the consumption of O_2 (C_{O2}, mol/s) at the reaction interface can be calculated by using the Faraday electrolysis law as below:[69]

$$C_{O_2} = \frac{j\eta S}{nF} \quad \text{(S4)}$$

where j is the current density (A/cm^2), η is the CE for H_2O_2 production (%), S is the electrode effective area (cm^2), n is the number of electrons transferred for O_2 reduction to H_2O_2 (n = 2), and F is the Faraday constant (96486 C/mol). According to the data in Fig. 3(e) of the main text, it can be calculated that C_{O2} corresponding to the "CCP + GDL" and "DCP + GDL" electrode is 1.0114 × 10^{-6} mol/s and 1.0619 × 10^{-6} mol/s at 30 mA/cm^2 (the first cycle), respectively. Next, in order to simplify the calculation model, we assume that there is no O_2 diffusion boundary layer inside the electrode. With the ideal gas law, the O_2 pressure difference (ΔP) between electrode reaction interface and surrounding air can be obtained:

$$\Delta P = \frac{\Delta nRT}{V} \quad \text{(S5)}$$

where Δn is the change of O_2 content in the electrode per unit time (approximate to the value of C_{O2}), R is the molar gas constant (8.314 J/(mol·K)), T is the gas temperature (298.15 K), and V is the volume change during O_2 consumption process (here represented by the electrode volume, in fact this value will be smaller due to the ultra-thin reaction interface). We can finally calculate the O_2 pressure difference of about 10918.73 Pa ("CCP + GDL") and 5285.66 Pa ("DCP + GDL") per unit reaction

time. Based on the CE >90% at the first cycle for both electrode configurations presented in Fig. 3(e) of the main text, we can safely conclude that the calculated values are high enough to drive the O_2 self-diffusion process. In addition, it needs to be clarified that the real O_2 pressure difference at the active interface may be greater than 10918.73 Pa or 5285.66 Pa, since the above calculation process does not involve the O_2 consumed by the $4e^-$ ORR pathway as a parasitic reaction (or equal to 10918.73 Pa or 5285.66 Pa if only hydrogen evolution side reaction occurs without $4e^-$ ORR).

Text S3. Calculation of capillary pressure driven electrolyte wetting electrode pores.

We first constructed the underwater DCP electrode model as shown in Fig. S27a and assumed that the nanopores in the dense region and the microchannels in the crack region are both perpendicular to the electrode surface, just like capillaries. The migration behavior of the liquid in the capillary is mainly related to the formation of a curved liquid surface and the resulting additional pressure (ΔP). The physical meaning of ΔP refers to the pressure difference between the non-wet phase and the wet phase on both sides of the curved liquid surface, which is also called capillary pressure (P_c) in the capillary, and its specific value can be calculated according to the Young-Laplace equation:[70]

$$\Delta P = P_c = \sigma(\frac{1}{R_1} + \frac{1}{R_2}) \quad \text{(S6)}$$

where σ is the surface tension of the liquid, and R_1 and R_2 are the radius of curvature of the curved liquid surface in two directions (Fig. S27b). Note that the direction of capillary force in our DCP model depends on the wetting properties of the electrodes. The capillary force points towards the liquid side and the gas side for hydrophobic and hydrophilic interfaces, respectively, given that the action direction of the capillary force always points to the concave side of the curved liquid surface. Considering the huge difference in pore shape between the dense region and the crack region of the DCP electrode, we simplified these two types of pores into cylindrical and square capillaries, respectively. For a cylindrical capillary (Fig. S27c), assuming that the curved liquid surface is part of the spherical surface, then $R_1 = R_2$, so the equation S6 can be written as:

$$P_c = \frac{2\sigma}{R} \quad \text{(S7)}$$

where R is the mean radius of curvature of the spherical surface, which is related to the contact angle (θ) and capillary radius (r) as:

$$R = \frac{r}{\cos\theta} \quad \text{(S8)}$$

Combining equations S7 and S8 yields:

$$P_c(dense\ region) = \frac{2\sigma\cos\theta}{r} \quad \text{(S9)}$$

For a square capillary, the liquid presents a horizontal surface on side α but a curved liquid surface on side β (Fig. S27d). This situation can be regarded as a series of cylindrical capillaries juxtaposed together. Similarly, assuming that the curved arc is part of a sphere, then $R_2 = \infty$, the P_c at the crack can therefore be calculated as:

$$P_c = \frac{\sigma}{R_1} \quad \text{(S10)}$$

R_1 is related to θ and crack width (b) as:

$$R_1 = \frac{\frac{b}{2}}{\cos\theta} \quad \text{(S11)}$$

Combining equations S10 and S11 yields:

$$P_c(crack\ region) = \frac{2\sigma\cos\theta}{b} \quad \text{(S12)}$$

In other words, our results demonstrate that the P_c of a square capillary of width b is equal to that of a cylindrical capillary of radius b. The average pore radius and width corresponding to the dense and crack regions were determined to be 68.2 nm and 138.4 μm, respectively, by using ImageJ software. The σ of Na_2SO_4 dilute electrolyte

(0.05 M) can be replaced by the surface tension of water (0.072 N/m). Based on the above analysis, we calculated the P_c as a function of the electrode contact angle in the dense and crack regions as follows, and the results are visualized in Fig. 4(d) of the main text.

$$P_c(dense\ region) = 2.11 \times 10^6 \times \cos\theta \quad \text{(S13)}$$

$$P_c(crack\ region) = 1.04 \times 10^3 \times \cos\theta \quad \text{(S14)}$$

With the application of the electric field, as discussed in the main text, the triggered electrowetting will continuously hydrophilize the electrode surface. Once the contact angle is less than 90°, the capillary force points towards the gas side, causing the liquid to spontaneously penetrate and wet the entire pore. Apparently, the advancing depth of the liquid in the dense region and the crack region is different due to the difference in the capillary driving force. In the simplified calculation model shown in Fig. S27e, when the liquid column pressure and capillary pressure are balanced, a steady state is reached, and the rising height of the liquid in the capillary can be derived according to hydrostatics as follows:

$$P_c = (\rho_{liquid} - \rho_{gas})gh \quad \text{(S15)}$$

$$h(dense\ region) = \frac{2\sigma\cos\theta}{\Delta\rho g r} \quad \text{(S16)}$$

$$h(crack\ region) = \frac{2\sigma\cos\theta}{\Delta\rho g b} \quad \text{(S17)}$$

where $\Delta\rho$ is the density difference between the liquid and the gas (approximately the density of water here), and g is the gravitational acceleration. This result indicates that under the same wettability, the depth of water immersion in the dense region is 2030

times higher than that in the crack region. We assume in the main text that the electrolyte floods one-third of the thickness of the dense region of the DCP electrode during electrolysis. Note that this is the case in an ideal cylindrical pore. In practice, however, the actual shape of the electrode pore is extremely irregular, which means that the advancement of water in the pores may be terminated when encountering a re-entrant cavity with a greater curvature due to the increased critical burst-through pressure. In fact, we did not find significant penetration of the electrolyte in the dense region of DCP (24.88 mg/cm^2) during the experiment.

Movie S1 and S2. Bubble evolution behavior on the electrolyte-facing side of the CCP (Movie S1) or DCP electrode (Movie S2) under pure O_2 aeration operation.

When pure O_2 gas was introduced into the additionally deployed gas chamber in the electrolysis system, uniform O_2 bubbles were observed to appear on the surface of the electrolyte-facing side of the CCP electrode. This stronger O_2 convection is beneficial to increase the local O_2 concentration at the electrowetting interface of the CCP electrode, thereby achieving the recovery of its H_2O_2 production performance. For the DCP electrode, the bubbles formed were significantly larger in size and faster in the formation rate than in the case of CCP, albeit at the same O_2 flow rate. This is because the DCP electrode allows preferential and rapid mass transfer of O_2 to the electrolyte via its internal micron-scale cracks, where approaching small bubbles will merge to form more irregular large bubbles. The above phenomenon also indirectly demonstrates that the DCP electrode is obviously superior to the CCP electrode in terms of gas mass transfer, corresponding to the experimental results in the main text. Note that the silver mirror-like reflection phenomenon at the crack is not observed in the case of DCP electrode, which is due to visual deviation caused by the vertical viewing angle.

References

S1 L. Cui, X. Zhao, H. Xie and Z. Zhang, *ACS Catal.*, 2022, **12**, 13334–13348.

S2 C. Zhang, J. Sha, H. Fei, M. Liu, S. Yazdi, J. Zhang, Q. Zhong, X. Zou, N. Zhao, H. Yu, Z. Jiang, E. Ringe, B. I. Yakobson, J. Dong, D. Chen and J. M. Tour, *ACS Nano*, 2017, **11**, 6930–6941.

S3 Z. Wang, Q.-K. Li, C. Zhang, Z. Cheng, W. Chen, E. A. McHugh, R. A. Carter, B. I. Yakobson and J. M. Tour, *ACS Catal.*, 2021, **11**, 2454–2459.

S4 M. Liu, Y. Pang, B. Zhang, P. De Luna, O. Voznyy, J. Xu, X. Zheng, C. T. Dinh, F. Fan, C. Cao, F. P. de Arquer, T. S. Safaei, A. Mepham, A. Klinkova, E. Kumacheva, T. Filleter, D. Sinton, S. O. Kelley and E. H. Sargent, *Nature*, 2016, **537**, 382–386.

S5 L. Martinez, R. Andrade, E. G. Birgin and J. M. Martinez, *J. Comput. Chem.*, 2009, **30**, 2157–2164.

S6 S. Plimpton, *J. Comput. Phys.*, 1995, **117**, 1–19.

S7 H. Heinz, T. J. Lin, R. K. Mishra and F. S. Emami, *Langmuir*, 2013, **29**, 1754–1765.

S8 S. Nosé, *Prog. Theor. Phys. Supp.*, 1991, **103**, 1–46.

S9 G. Liu, W. S. Y. Wong, M. Kraft, J. W. Ager, D. Vollmer and R. Xu, *Chem. Soc. Rev.*, 2021, **50**, 10674–10699.

S10 Z. Lu, W. Xu, J. Ma, Y. Li, X. Sun and L. Jiang, *Adv. Mater.*, 2016, **28**, 7155–7161.

S11 K. Kwon, J. O. Park, D. Y. Yoo and J. S. Yi, *Electrochim. Acta*, 2009, **54**, 6570–6575.

S12 Q. Chen, K. Liu, Y. Zhou, X. Wang, K. Wu, H. Li, E. Pensa, J. Fu, M. Miyauchi, E. Cortes and M. Liu, *Nano Lett.*, 2022, **22**, 6276–6284.

S13 W. Ge, Y. Chen, Y. Fan, Y. Zhu, H. Liu, L. Song, Z. Liu, C. Lian, H. Jiang and C. Li, *J. Am. Chem. Soc.*, 2022, **144**, 6613–6622.

S14 Z. Xing, L. Hu, D. S. Ripatti, X. Hu and X. Feng, *Nat. Commun.*, 2021, **12**, 136.

S15 Y. Li, H. S. Pillai, T. Wang, S. Hwang, Y. Zhao, Z. Qiao, Q. Mu, S. Karakalos, M. Chen, J. Yang, D. Su, H. Xin, Y. Yan and G. Wu, *Energy Environ. Sci.*, 2021, **14**, 1449–1460.

S16 W. Xu, Z. Lu, X. Sun, L. Jiang and X. Duan, *Acc. Chem. Res.*, 2018, **51**, 1590–1598.

S17 Z. Song, C. Xu, X. Sheng, X. Feng and L. Jiang, *Adv. Mater.*, 2018, **30**, 1701473.

S18 A. K. C. Wong, R. Banerjee and A. Bazylak, *J. Electrochem. Soc.*, 2019, **166**, F3009–F3019.

S19 Z. Xing, K. Shi, Z. S. Parsons and X. Feng, *ACS Catal.*, 2023, **13**, 2780–2789.

S20 P. Cao, X. Quan, K. Zhao, X. Zhao, S. Chen and H. Yu, *ACS Catal.*, 2021, **11**, 13797–13808.

S21 L. Cui, M. Sun and Z. Zhang, *Chem. Eng. J.*, 2022, **450**, 138263.

S22 Y.-y. Gu, H. Fu, Z. Huang, R. Lin, Z. Wu, M. Li, Y. Cui, R. Fu and S. Wang, *J. Clean. Prod.*, 2022, **341**, 130799.

S23 M. Li, X. Qin, M. Gao, T. Li and Y. Lv, *Environ. Sci.: Nano*, 2022, **9**, 632–652.

S24 A. Xu, B. He, H. Yu, W. Han, J. Li, J. Shen, X. Sun and L. Wang, *Electrochim. Acta*, 2019, **308**, 158–166.

S25 Y. Zhu, S. Qiu, F. Ma, G. Li, F. Deng and Y. Zheng, *Electrochim. Acta*, 2018, **261**, 375–383.

S26 L. Cui, P. Ding, M. Zhou and W. Jing, *Chem. Eng. J.*, 2017, **330**, 1316–1325.

S27 Y. Sun, L. Silvioli, N. R. Sahraie, W. Ju, J. Li, A. Zitolo, S. Li, A. Bagger, L. Arnarson, X. Wang, T. Moeller, D. Bernsmeier, J. Rossmeisl, F. Jaouen and P. Strasser, *J. Am. Chem. Soc.*, 2019, **141**, 12372–1325.

S28 Z. Ye, D. R. V. Guelfi, G. Álvarez, F. Alcaide, E. Brillas and I. Sirés, *Appl. Catal., B*, 2019,

247, 191–199.

S29 J. Lu, X. Liu, Q. Chen and J. Zhou, *Sep. Purif. Technol.*, 2021, **265**, 118493.

S30 F. Alcaide, G. Álvarez, D. R. V. Guelfi, E. Brillas and I. Sirés, *Chem. Eng. J.*, 2020, **379**, 122417.

S31 W. Li, Y. Feng, J. An, L. Yunfei, Q. Zhao, C. Liao, X. Wang, J. Liu and N. Li, *Environ. Res.*, 2022, **204**, 112327.

S32 X. Lu, M. Zhou, Y. Li, P. Su, J. Cai and Y. Pan, *Electrochim. Acta*, 2019, **320**, 134552.

S33 H. Yang, M. Zhou, W. Yang, G. Ren and L. Ma, *Chemosphere*, 2018, **206**, 439–446.

S34 E. Zhang, L. Tao, J. An, J. Zhang, L. Meng, X. Zheng, Y. Wang, N. Li, S. Du, J. Zhang, D. Wang and Y. Li, *Angew. Chem. Int. Ed.*, 2022, **61**, e202117347.

S35 H. Li, P. Wen, D. S. Itanze, Z. D. Hood, S. Adhikari, C. Lu, X. Ma, C. Dun, L. Jiang, D. L. Carroll, Y. Qiu and S. M. Geyer, *Nat. Commun.*, 2020, **11**, 3928.

S36 C. Liu, H. Li, F. Liu, J. Chen, Z. Yu, Z. Yuan, C. Wang, H. Zheng, G. Henkelman, L. Wei and Y. Chen, *J. Am. Chem. Soc.*, 2020, **142**, 21861–21871.

S37 E. Jung, H. Shin, B. H. Lee, V. Efremov, S. Lee, H. S. Lee, J. Kim, W. Hooch Antink, S. Park, K. S. Lee, S. P. Cho, J. S. Yoo, Y. E. Sung and T. Hyeon, *Nat. Mater.*, 2020, **19**, 436–442.

S38 Z. Lu, G. Chen, S. Siahrostami, Z. Chen, K. Liu, J. Xie, L. Liao, T. Wu, D. Lin, Y. Liu, T. F. Jaramillo, J. K. Nørskov and Y. Cui, *Nat. Catal.*, 2018, **1**, 156–162.

S39 Y. Wang, R. Shi, L. Shang, G. I. N. Waterhouse, J. Zhao, Q. Zhang, L. Gu and T. Zhang, *Angew. Chem. Int. Ed.*, 2020, **59**, 13057–13062.

S40 Y. Wang, R. Shi, L. Shang, L. Peng, D. Chu, Z. Han, G. I. N. Waterhouse, R. Zhang and T. Zhang, *Nano Energy*, 2022, **96**, 107046.

S41 J. Wu, M. Hou, Z. Chen, W. Hao, X. Pan, H. Yang, W. Cen, Y. Liu, H. Huang, P. W. Menezes and Z. Kang, *Adv. Mater.*, 2022, **34**, e2202995.

S42 S. Chen, T. Luo, X. Li, K. Chen, J. Fu, K. Liu, C. Cai, Q. Wang, H. Li, Y. Chen, C. Ma, L. Zhu, Y. R. Lu, T. S. Chan, M. Zhu, E. Cortes and M. Liu, *J. Am. Chem. Soc.*, 2022, **144**, 14505–14516.

S43 S. Chen, T. Luo, K. Chen, Y. Lin, J. Fu, K. Liu, C. Cai, Q. Wang, H. Li, X. Li, J. Hu, H. Li, M. Zhu and M. Liu, *Angew. Chem. Int. Ed.*, 2021, **60**, 16607–16614.

S44 W. Zhou, X. Meng, L. Rajic, Y. Xue, S. Chen, Y. Ding, K. Kou, Y. Wang, J. Gao, Y. Qin and A. N. Alshawabkeh, *Electrochem. Commun.*, 2018, **96**, 37–41.

S45 X. Tan, C. Jin, W. Sun, Y. Zhao, H. Wei and C. Sun, *Chemosphere*, 2021, **275**, 130060.

S46 X. Yu, M. Zhou, G. Ren and L. Ma, *Chem. Eng. J.*, 2015, **263**, 92–100.

S47 J. An, N. Li, Q. Zhao, Y. Qiao, S. Wang, C. Liao, L. Zhou, T. Li, X. Wang and Y. Feng, *Water Res.*, 2019, **164**, 114933.

S48 Q. Zhao, J. An, S. Wang, Y. Qiao, C. Liao, C. Wang, X. Wang and N. Li, *ACS Appl. Mater. Interfaces*, 2019, **11**, 35410–35419.

S49 D. Li, T. Zheng, Y. Liu, D. Hou, K. K. Yao, W. Zhang, H. Song, H. He, W. Shi, L. Wang and J. Ma, *J. Hazard. Mater.*, 2020, **396**, 122591.

S50 Y. Gu, S. Wu, Y. Cao, M. Liu, S. Chen, X. Quan and H. Yu, *ACS Appl. Mater. Interfaces*, 2021, **13**, 56045–56053.

S51 V. Poza-Nogueiras, Á. Moratalla, M. Pazos, Á. Sanromán, C. Sáez and M. A. Rodrigo, *Chem. Eng. J.*, 2022, **431**, 133280.

S52 Y. Zhao, N. Deng, Z. Fan, Z.-T. Hu, L. Fan, J. Zhou and X. Huang, *Chem. Eng. J.*, 2022, **430**,

132829.
S53 Q. Zhang, M. Zhou, G. Ren, Y. Li, Y. Li and X. Du, *Nat. Commun.*, 2020, **11**, 1731.
S54 J. An, Y. Feng, N. Wang, Q. Zhao, X. Wang and N. Li, *J. Hazard. Mater.*, 2022, **428**, 128185.
S55 C. Xia, Y. Xia, P. Zhu, L. Fan and H. Wang, *Science*, 2019, **366**, 226–231.
S56 S. Wang, D. Ye, H. Liu, X. Zhu, Q. Lan, Y. Yang, R. Chen and Q. Liao, *Sep. Purif. Technol.*, 2022, **297**, 121527.
S57 Y. Sheng, Y. Zhao, X. Wang, R. Wang and T. Tang, *Electrochim. Acta*, 2014, **133**, 414–421.
S58 X. Zhang, X. Zhao, P. Zhu, Z. Adler, Z. Y. Wu, Y. Liu and H. Wang, *Nat. Commun.*, 2022, **13**, 2880.
S59 C. Yang, F. Sun, Z. Qu, X. Li, W. Zhou and J. Gao, *ACS Energy Lett.*, 2022, **7**, 4398–4407.
S60 H. Li, E. Quispe-Cardenas, S. Yang, L. Yin and Y. Yang, *ACS EST Engg.*, 2022, **2**, 242–250.
S61 S. C. Perry, D. Pangotra, L. Vieira, L.-I. Csepei, V. Sieber, L. Wang, C. Ponce de León and F. C. Walsh, *Nat. Rev. Chem.*, 2019, **3**, 442–458.
S62 W. Wang, X. Lu, P. Su, Y. Li, J. Cai, Q. Zhang, M. Zhou and O. Arotiba, *Chemosphere*, 2020, **259**, 127423.
S63 W. Peng, J. Liu, X. Liu, L. Wang, L. Yin, H. Tan, F. Hou and J. Liang, *Nat. Commun.*, 2023, **14**, 4430.
S64 Y. Lin, T. Wang, L. Zhang, G. Zhang, L. Li, Q. Chang, Z. Pang, H. Gao, K. Huang, P. Zhang, Z. J. Zhao, C. Pei and J. Gong, *Nat. Commun.*, 2023, **14**, 3575.
S65 J. Gu, S. Liu, W. Ni, W. Ren, S. Haussener and X. Hu, *Nat. Catal.*, 2022, **5**, 268–276.
S66 J. E. Huang, F. Li, A. Ozden, A. Sedighian Rasouli, F. P. García de Arquer, S. Liu, S. Zhang, M. Luo, X. Wang, Y. Lum, Y. Xu, K. Bertens, R. K. Miao, C.-T. Dinh, D. Sinton and E. H. Sargent, *Science*, 2021, **372**, 1074–1078.
S67 C.-T. Dinh, T. Burdyny, M. Golam Kibria, A. Seifitokaldani, C. M. Gabardo, F. P. García de Arquer, A. Kiani, J. P. Edwards, P. De Luna, O. S. Bushuyev, C. Zou, R. Quintero-Bermudez, Y. Pang, D. Sinton and E. H. Sargent, *Science*, 2018, **360**, 783–787.
S68 H.-Q. Liang, S. Zhao, X.-M. Hu, M. Ceccato, T. Skrydstrup and K. Daasbjerg, *ACS Catal.*, 2021, **11**, 958–966.
S69 G. Xia, Y. Tian, X. Yin, W. Yuan, X. Wu, Z. Yang, G. Yu, Y. Wang and M. Wu, *Appl. Catal., B*, 2021, **299**, 120655.
S70 K. Yang, R. Kas, W. A. Smith and T. Burdyny, *ACS Energy Lett.*, 2020, **6**, 33–40.